CLOUD SYSTEM EVOLUTION IN THE TRADES (CSET)

Following the Evolution of Boundary Layer Cloud Systems with the NSF–NCAR GV

Bruce Albrecht, Virendra Ghate, Johannes Mohrmann, Robert Wood, Paquita Zuidema, Christopher Bretherton, Christian Schwartz, Edwin Eloranta, Susanne Glienke, Shaunna Donaher, Mampi Sarkar, Jeremy McGibbon, Alison D. Nugent, Raymond A. Shaw, Jacob Fugal, Patrick Minnis, Robindra Paliknoda, Louis Lussier, Jorgen Jensen, J. Vivekanandan, Scott Ellis, Peisang Tsai, Robert Rilling, Julie Haggerty, Teresa Campos, Meghan Stell, Michael Reeves, Stuart Beaton, John Allison, Gregory Stossmeister, Samuel Hall, and Sebastian Schmidt

The evolution of the boundary layer aerosol, cloud, precipitation, and thermodynamic structures along trajectories within the North Pacific trade winds was investigated using the NSF–NCAR Gulfstream V.

Boundary layer clouds in the form of stratocumulus and small marine cumulus are the most frequently observed cloud types over the Earth's oceans, are the most abundant types globally (Norris 1998), and have an important impact on the Earth's radiation budget (Hartmann and Short 1980). The energy and moisture fluxes associated with these clouds are critical in maintaining the thermodynamic structure of the lower troposphere. Thus, both the turbulent mixing and the radiative impact on the surface associated with marine boundary layer (MBL) clouds need to be adequately parameterized in large-scale models (Bony and Dufresne 2005). The inadequate representation of MBL cloud processes in large-scale models continues to be a major contributor to model uncertainties in cloud feedback representations—particularly in subtropical anticyclone regions (Zhang et al. 2005; Wyant et al. 2010; Teixeira et al. 2011; Soden and Vecchi 2011).

The stratocumulus (Sc) regimes associated with the eastern flank of the subtropical anticyclones evolve into fair-weather cumulus (Cu) regimes in the persistent trade winds associated with the anticyclones (Wood 2012). The high albedo and large areal extent of Sc induce a significant reduction in surface solar heating (e.g., Hartmann et al. 1992; Klein and Hartmann 1993). Cumuli, on the other hand, play a fundamental role in the regulation of ocean surface evaporation and convergence of moisture into deep convective regions (e.g., Tiedtke 1989; Neggers et al. 2007), and therefore the global hydrological cycle. The transition from shallow cloud-topped MBLs in the cool subtropics to broken trade cumulus over the warm tropics (Bretherton and Wyant 1997; Wyant et al. 1997; Sandu and Stevens 2011) occurs over all subtropical ocean basins and sets the climatological distribution of cloud cover (Albrecht et al. 1995a). In the Sc–Cu transition, the MBL evolves from a well-mixed single layer topped with extensive clouds under a sharp inversion into a deeper, vertically stratified structure containing cumulus clouds with greatly reduced cover capped by a weaker and more diffuse inversion.

Cloud-top entrainment is one of the key processes driving the stratocumulus-to-cumulus transition. The MBL deepening associated with entrainment causes decoupling: the separation of the MBL into two distinct layers with limited exchange between them, an exchange that is mediated by the cumulus rooted in the lower surface-based mixed layer. Decoupling starves the Sc of their surface moisture source, while the continuing entrainment of dry air into the MBL caused by the more energetic cumulus plumes leads to the breakup of the Sc. They are replaced by broken Cu, whose tops are more variable, with a greater spread of cloud-top height and fewer reaching the inversion. Cloud-top entrainment profoundly impacts the type and coverage of clouds within the MBL because it plays such an important role in the MBL moisture, heat, and momentum budgets (Lilly 1968; Bretherton and Wyant 1997; Wyant et al. 1997; Stevens 2002; Stevens et al. 2002). In addition, cloud-top entrainment controls how MBL clouds respond to increased greenhouse gases (Caldwell and Bretherton 2009) and atmospheric aerosols (Ackerman et al. 2004; Wood 2007; Bretherton et al. 2007).

Precipitation can also hasten the stratocumulus-to-cumulus transition (Yamaguchi et al. 2017; Abel et al. 2017). Both the cloud depth and the aerosol cloud condensation nuclei (CCN) concentrations can impact the initiation of precipitation. Thus, entrainment growth of the boundary layer depth is a factor in the development of drizzle. The subsequent removal of aerosols by the precipitation maintains an environment of enhanced precipitation susceptibility. This feedback between the aerosol removal and the precipitation enhancement increases the rate at which the cloudiness can decrease (Yamaguchi et al. 2017). Thus, cloud–aerosol–precipitation interactions can play an important role in the rate at which the transition occurs.

Cloud System Evolution in the Trades (CSET) was developed to describe and explain the evolution of the MBL aerosol, cloud, and thermodynamic structures along trajectories within the North Pacific trade winds using the National Science Foundation–National Center for Atmospheric Research (NSF–NCAR) Gulfstream V [GV; also known as High-Performance Instrumented Airborne Platform for Environmental Research (HIAPER)] on flights between California and Hawaii. The long range and endurance of the NSF GV allowed for the sampling of air masses on low-level trajectories extending from California to Hawaii and then a resampling of these same air masses on the return flight two days later.

The stratocumulus–trade cumulus transition is often sharply defined, as shown in Fig. 1. The upstream part of the transition was arguably first examined with five NCAR Electra flights undertaken in 1975 and documented in Brost et al. (1982a,b) and Albrecht et al. (1985). The Atlantic Stratocumulus Transition Experiment (ASTEX; Albrecht et al. 1995b) brought new cloud remote sensors to the field as well as an explicit Lagrangian sampling approach. Two Lagrangian experiments tracked air masses for 36–48 h using instrumented aircraft (Bretherton and Pincus 1995; Bretherton et al. 1995). The ASTEX Lagrangian studies, however, were not made in classic trade wind flow conditions and lacked the aircraft-based lidar and radar observations needed to provide a detailed mapping of cloud and precipitation structures.

More recent regional observational and modeling studies have also focused on the MBL cloud, aerosol, and precipitation structures in cloud regimes associated with the transition. During the Variability of American Monsoon Systems (VAMOS) Ocean–Cloud–Atmosphere–Land Study Regional

AFFILIATIONS: Albrecht, Zuidema, and Sarkar—Department of Atmospheric Sciences, University of Miami, Miami, Florida; Ghate and Schwartz—Argonne National Laboratory, Lemont, Illinois; Mohrmann, Wood, Bretherton, and McGibbon—Department of Atmospheric Sciences, University of Washington, Seattle, Washington; Eloranta—University of Wisconsin–Madison, Madison, Wisconsin; Glienke and Shaw—Atmospheric Sciences Program, Michigan Technological University, Houghton, Michigan; Donaher—Emory University, Atlanta, Georgia; Nugent—Department of Atmospheric Sciences, University of Hawai‘i at Mānoa, Honolulu, Hawaii; Fugal—Max Planck Institute of Chemistry, Mainz, Germany; Minnis and Palikonda—Science Systems and Applications, Inc., Lanham, Maryland, and NASA Langley Research Center, Hampton, Virgina; Lussier, Jensen, Vivekanandan, Ellis, Tsai, Rilling, Haggerty, Stell, Reeves, Beaton, Allison, Stossmeister, and Hall—Earth Observing Laboratory, NCAR, Boulder, Colorado; Campos—Atmospheric Chemistry Observations and Modeling Laboratory, NCAR, Boulder, Colorado; Schmidt—University of Colorado Boulder, Boulder, Colorado

CORRESPONDING AUTHOR: Bruce Albrecht, balbrecht@miami.edu

The abstract for this article can be found in this issue, following the table of contents.
DOI:10.1175/BAMS-D-17-0180.1

In final form 10 July 2018

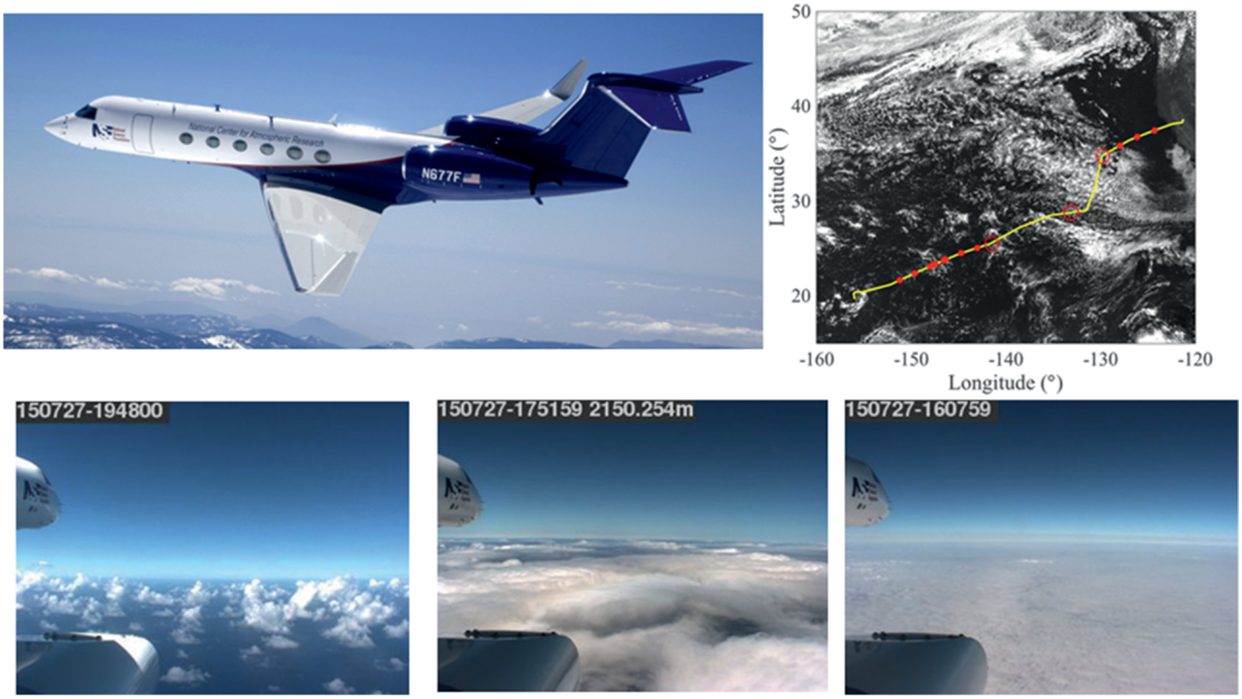

Fig. 1. (top left) Photo of NSF–NCAR GV and (top right) GOES visible image with aircraft path on 27 Jul 2015 RF10 during CSET. The red points indicate where dropsonde launches were made. (bottom) Photos from this flight were taken by a camera mounted on the starboard/right wing of the GV. Shown are clouds observed along the flight path in the downstream direction (east to west) from (right) unbroken uniform stratus to (middle) mesoscale complexes to (left) shallow cumuli.

Experiment (VOCALS-REx; 2008), a comprehensive study was made of the aerosol, cloud, and precipitation properties of stratocumulus clouds in the southeastern Pacific (Wood et al. 2011a; Mechoso et al. 2014). The observational and modeling studies focused on the stratocumulus structures extending westward from the west coast of Chile. The VOCALS studies have brought important new insight into the extreme aerosol–cloud interactions associated with pockets of open cells (POCs) and the role of mesoscale organizations in those interactions (Wood et al. 2011b; Berner et al. 2011; Kazil et al. 2011; Wang et al. 2010; Berner et al. 2013). In addition, VOCALS provided a comprehensive description of the aerosol, cloud, precipitation, and MBL structures as the MBL deepens along 20°S for ~1,500 km westward from the Chilean coast (Bretherton et al. 2010a). The VOCALS results provide an important baseline for comparing the microphysical and macrophysical structures of the clouds sampled during CSET.

VOCALS did not extend into the trade wind cumulus regime downwind of the main Sc deck. Much of the early observational work on small cumuli in the trade wind boundary layer was conducted using in situ aircraft observations. But there are inherent limitations to this approach, since the volume sampled during an aircraft penetration is relatively small and it is difficult to study the time evolution of the vertical structure. Furthermore, it is difficult to determine exactly where in the cloud the measurements are being made and what stage of the cloud life cycle is being sampled. During the Rain in Cumulus over the Ocean (RICO; Rauber et al. 2007) field campaign, some important issues were addressed concerning aerosol–cloud interactions (e.g., Gerber et al. 2008); however, the RICO aircraft measurements did not benefit from good cloud radar observations. During the Barbados Aerosol Cloud Experiment (BACEX; 2010), in situ cloud observations in fair-weather cumulus clouds were made with the Center for Interdisciplinary Remotely-Piloted Aircraft Studies (CIRPAS) Twin Otter research aircraft (Jung et al. 2016) and with an upward-pointing frequency-modulated continuous-wave (FMCW) cloud radar. The RICO and BACEX observations provided insight into entrainment and precipitation processes in liquid-only cumulus clouds (e.g., Nuijens et al. 2009; Minor et al. 2011; Zuidema et al. 2012a), and a background for the CSET observations in the fair-weather cumulus regions sampled.

Although recent field programs have advanced our understanding of processes operating in the two cloud regimes central to CSET, they have not directly addressed the transition from stratocumulus to trade cumulus. A recent study, the Marine Atmospheric Radiation Measurement (ARM) Global Energy and Water Cycle Experiment (GEWEX) Cloud System Study (GCSS) Pacific Cross-Section Intercomparison (GPCI) Investigation of Clouds (MAGIC), involved shipborne measurements from a container ship that made regular transects between Los Angeles and Hawaii from October 2012 to September 2013 using the Department of Energy's (DOE's) ARM Mobile Facility (Zhou et al. 2015). In addition to in situ observations, the clouds above the ship were sampled using lidar and radar observations in both the stratocumulus and the trade cumulus regime. Although the cloud transition is well defined in some transects, the slow movement of the ship limits the usefulness of these observations for Lagrangian studies.

The subtropical northeastern Pacific stratocumulus-to-cumulus transition sampled during CSET flights has long been a canonical modeling challenge. Two benchmark cases of Sc–Cu transition have been used for international modeling intercomparison efforts as part of the Global Atmospheric System Study (GASS) and its predecessor, GCSS. The first of these was from the 1992 ASTEX project, which was conducted over the northeast Atlantic Ocean, described previously (Bretherton et al. 1995, 1999; van der Dussen et al. 2013). The second was a satellite-derived composite (Sandu et al. 2010; de Roode et al. 2016) of several thousand Lagrangian trajectories based on Moderate Resolution Imaging Spectroradiometer (MODIS) cloud observations with trajectories based on European Centre for Medium-Range Weather Forecasts (ECMWF) reanalyses. Neither case includes a good accompanying set of aerosol observations in or above the boundary layer or the robust statistics on horizontal cloud and precipitation inhomogeneity that a cloud radar and lidar combination can provide (e.g., Bretherton et al. 2010b; Wood et al. 2011b).

Large-eddy simulation (LES) models have become a robust tool for Lagrangian simulations of subtropical cloudiness transitions, but there are few good datasets for comprehensively testing these simulations. In particular, we lack adequate observations of the coupled evolution of aerosol, cloud droplet number concentration, and precipitation during such transitions. The MAGIC ARM Mobile Facility (AMF) deployment provided a ship-based perspective on this problem (McGibbon and Bretherton 2017; Zhou et al. 2015), but the long range of the GV allows in situ measurements of aerosols and cloud microphysics, including interactions with the free troposphere, across the entire transition. By resampling the same boundary layer air masses on the return flights as the outbound flights, the measurements can be naturally compared with the Lagrangian LES, which have proved to be valuable for constructing and analyzing better models of MBL cloud and its sensitivity to environmental conditions. The Eulerian and Lagrangian samplings from CSET also provide valuable datasets for directly evaluating forecast models and general circulation models (GCMs) used in forecast mode.

Based on this background, the following scientific goals were determined for CSET:

- Define the evolution of the cloud, precipitation, and aerosol fields in stratocumulus clouds as they transition into the fair-weather cumulus regimes within the subtropical easterlies over the northern Pacific.
- Examine the cloud microphysical properties and processes as a function of boundary layer depth, toward assessing the relative contributions of internal processes (e.g., entrainment, turbulence, and drizzle) and external forcing (e.g., sea surface temperature, winds, and subsidence) to boundary layer cloud system evolution.
- Evaluate the relative importance of boundary layer deepening and precipitation processes in driving boundary layer decoupling and cloud breakup.
- Provide comprehensive case studies and integrated datasets to evaluate and improve process models, LES, and GCMs to describe and explain cloud system evolution in the trades.

The observational effort included characterization of the cloud, precipitation, and aerosol fields in the stratocumulus and the fair-weather cumulus regimes within the subtropical easterlies over the northern Pacific. These characterizations along trajectories were designed to aid in our understanding and simulation of the transition between the two convective regimes. The Lagrangian approach allowed us to track air masses as they flowed from colder to warmer sea surface temperatures and thus minimize uncertainties in the large-scale forcing caused by horizontal advection in the lower troposphere. This approach facilitates comparison with Lagrangian model simulations and the isolation of critical physical processes operating in the cloud evolution.

EXPERIMENT DESIGN. The NSF–NCAR GV was selected for CSET because of its range and endurance and its observational capabilities. But since the GV range is substantially reduced when flown at lower levels because of slower air speeds, the amount of time that could be flown for low-level boundary sampling was limited to about 50% of the flight time between California and Hawaii. The instrumentation used on the GV allowed for a combination of in situ and remote sensing observations. The remote sensing observations were used both during the boundary layer sampling and the legs flown at higher altitudes.

Instrumentation. A full suite of probes on the GV were used for in situ measurements of aerosol, cloud, precipitation, and turbulence properties. The instrumentation is listed in Table 1 and described in detail on the Earth Observing Laboratory (EOL) website (https://archive.eol.ucar.edu/raf/instruments/doc/). The GV was well instrumented for making in situ characterizations of the mean and turbulent wind and thermodynamic structures below, in, and above the cloud layer. Further, aerosol, cloud, and precipitation observations (concentrations and size distributions) were made from the GV using several probes. The GV aerosol measurements were made using an ultrahigh-sensitivity aerosol spectrometer (UHSAS) that samples particles in the nominal range of 0.06–1.0 μm (but reduced to 0.075–1.0 μm for CSET). A condensation nuclei (CN) counter gives the total aerosol concentrations greater than a threshold of about 10 nm. The cloud particle size distributions were measured with a cloud droplet probe (CDP), and the precipitation-sized water droplet distributions were obtained using two-dimensional optical array probes for cloud and precipitation (OAP-2DC and OAP-2DP, respectively), with ranges spanning 50–3,000 μm. An important addition was the second-generation Holographic Detector for Clouds (HOLODEC; Fugal and Shaw 2009; Spuler and Fugal 2011), a new instrument used on the GV to size cloud and drizzle droplets in the range of about 6 μm–1 mm and to determine the three-dimensional position of hydrometeors using digital in-line holography. The unique aspects of HOLODEC are that the sample volume measured per second (about 43 cm^3) does not depend on aircraft speed and the effects produced by shattering from the aperture edges can be identified and eliminated. Most significantly, it is possible to measure cloud droplet size distributions from individual localized sample volumes with the largest horizontal dimension being 130 mm, instead of an average over more than 10 m for optical array probes (e.g., for a measurement from a CDP at 10 Hz), as well as to determine the positions of the droplets within that volume. Postflight analyses of the holograms recorded at 3.3 Hz produced cloud and precipitation size distributions during CSET (Glienke et al. 2017).

Ozone and carbon monoxide measurements were made using the fast-response ozone (F03 AD) and carbon monoxide [Aero-Laser vacuum ultraviolet (VUV)] instruments supported by the Community Airborne Research Instrumentation (CARI) group in the Atmospheric Chemistry Observations and Modeling (ACOM) section of NCAR. Upward and downward longwave (LW) and upward shortwave (SW) radiative fluxes were measured by Kipp and Zonen broadband radiometers; the HIAPER Airborne Radiation Package (HARP) provided upward and downward shortwave spectral irradiances.

Two key remote sensing systems used on the GV during CSET were the HIAPER Cloud Radar (HCR) developed by NCAR EOL and the high-spectral-resolution lidar (HSRL) developed under the NSF HIAPER Aircraft Instrumentation Solicitation (HIAS). These remote sensing systems were used to define macroscopic and microscopic cloud properties as the GV flew above, below, and in the clouds. The HCR characteristics are described in Rauber et al. (2017) and in Schwartz et al. (2018, manuscript submitted to *J. Atmos. Oceanic Technol.*). It is a pulsed Doppler radar that operates at a 94-GHz frequency (3.2-mm wavelength) and has a sensitivity of −39.6 dBZ at 1-km range. The HCR in CSET was operated with a temporal resolution of 0.5 s, which for airspeeds of the GV gives a horizontal resolution of 50–100 m. The vertical range resolution of 20 m makes the HCR ideal for observing stratocumulus and cumulus clouds and their associated precipitation structures. The first three Doppler spectra moments (reflectivity, mean Doppler velocity, and spectral width), calculated using the pulse-pair technique, were displayed in real time on the aircraft and recorded and archived for processing. In addition, the raw data that give phase and amplitude from the in-phase (I) and quadrature-phase (Q) signals for each pulse were recorded and archived for each flight. These raw I and Q data were used in postprocessing to calculate the full radar Doppler spectrum and its first four moments (Schwartz et al. 2018, manuscript submitted to *J. Atmos. Oceanic Technol.*).

A special wing pod was developed for mounting the HCR onto the GV (Fig. 2). The pod design allowed a steerable reflector to extend ahead of the wing to allow for sampling both below and above the aircraft. The reflector was also actively controlled to minimize pointing errors caused by pitch variations on the GV (Vivekanandan et al. 2015). Operating at 94-GHz frequency, the HCR suffers from small attenuation caused by absorption by water vapor and oxygen. Corrections (less than 1 dBZ km^{-1}) were made using

Table 1. GV Instrumentation for CSET.

Instrument or observing system	Parameters measured and range
Thermometer (102AL TAT)	Temperature
Dewpoint hygrometer (BUCK 1011C)	Dewpoint temperature
Vertical cavity surface emitting laser hygrometer (VCSEL)	Water vapor concentration
Winds (gust measurements; aircraft motion and position)	3D wind components
CDP	Cloud droplet spectra (2–50 μm)
Two-dimensional optical array probe (2DC)	Cloud and drizzle droplet spectra (60–3,200 μm)
HOLODEC	Cloud and drizzle (6 μm–1 mm)
UHSAS	Aerosol spectra (75–1,000 nm)
CN counter	Aerosol concentrations (>11 nm)
King probe	Cloud liquid water content
Heinmann infrared radiation pyrometer	Sea surface temperature
Microwave temperature profiler (MTP)	Vertical temperature profile
Broadband SW and LW radiometers (Kipp and Zonen)	Upward broadband shortwave irradiances, up and down infrared broadband irradiances
HARP	Upward and downward spectral shortwave irradiances
Digital cameras (on right and left wings)	Forward-looking images
AVAPS	Dropsonde signal processor
HCR (95 GHz)	Reflectivity, spectral width, Doppler velocity, raw *I* and *Q*
G-band microwave radiometer (183 GHz)	Liquid water path
HSRL	Backscatter and linear depolarization
Fast-response ozone (FO3_AD)	Ozone mixing ratio
Carbon monoxide (Aereo-Laser VUV)	Carbon monoxide
Dropsondes	Temperature, humidity, and wind profiles

dropsonde data obtained during CSET, based on the method described by Ulaby et al. (1981), when the radar is looking downward from above the clouds.

The HCR characterized the cloud and precipitation structures and provided a measure of cloud-top heights during both pointing directions. Its volume sampling is well suited for characterizing light precipitation—a highly localized and variable quantity (e.g., Wood 2005). Aircraft-based 95-GHz radar measurements have a proven track record for advancing our understanding of the role of precipitation in MBL clouds (Vali et al. 1998; Stevens et al. 2003; Wood et al. 2011a). Ground-based and airborne cloud radars have been used to characterize the vertical velocity structure of stratocumulus clouds (e.g., Lothon et al. 2005; Ghate et al. 2010) and of shallow cumulus clouds (e.g., Geerts and Miao 2005; Ghate et al. 2011; Wang and Geerts 2013). During nonprecipitating conditions (reflectivity < −15 dB*Z*) when the cloud droplets have negligible fall velocity, the measured Doppler velocity corrected for the aircraft motion can be used as a proxy for the vertical air motion (Lothon et al. 2005). During precipitating conditions, either (a) the fall velocity of precipitating drops can be removed from the measured Doppler velocity corrected for the aircraft motion to retrieve the vertical air motion or (b) the method proposed by Luke and Kollias (2013) that uses the higher-order moments of radar Doppler spectrum can distinguish between the echoes caused by cloud droplets and drizzle drops and can be used to calculate the vertical air motion. Also, when drops larger than 1.6 mm in diameter exist in the radar sample volume, a "notch" in the Doppler spectrum can be observed (Kollias et al. 2002) as a result of scattering by the drops in the Mie regime. The presence of the Mie notch allows the retrieval of air vertical velocity (e.g., Kollias et al. 2002; Giangrande et al. 2012; Fang et al. 2017). Mie notches were observed frequently during CSET and will be used to deduce vertical air motions in more heavily precipitating clouds using the HCR.

The HSRL used in CSET is an eye-safe calibrated lidar system that measures backscatter cross-sectional, extinction, and depolarization properties of atmospheric aerosols and clouds (Razenkov et al. 2002; Eloranta et al. 2008). The HSRL provides estimates of

Fig. 2. Photos of (top) HCR on the wing of GV and (bottom) HSRL pointing (left) up and (right) down inside the GV.

EOL FIELD CATALOG

One of the data support services made available for field campaigns by NCAR/EOL is the field catalog (http://catalog.eol.ucar.edu/). The field catalog is a suite of tools that is customized for each field campaign to provide support for the documentation of observational field project operations, mission planning, cross-project collaboration, real-time situational awareness, communication with and direction of remote instrument platforms, and postoperations product review and playback (Fig. SB1).

PROJECT DOCUMENTATION. The field catalog provides reporting tools for documenting project operations. These tools allow users to upload Portable Document Format (PDF) files or write reports in their web browser and to include special formatting, in-line images, URLs, instrument status, and event-specific information. A typical field catalog includes daily operation plans, weather forecast/summaries, and instrument status tables. Other reports that are generated on an as-needed basis may include flight plans, debrief reports, instrument/platform mission summaries, operations summaries, instrument logs, chemical forecasts/discussions, and nowcasts. The field catalog also includes a mission table that summarizes all of the major events and operations that occurred during the field campaign.

SUPPORTING PRODUCTS. The EOL data management team works with the project principal investigators (PIs) to determine beforehand a list of necessary products that should be collected and available in real time for the field campaign. This list includes necessary information for real-time decision-making as well as for documentation of conditions in which the research data were collected. The field catalog also collects any research products generated in the field that the project participants provide. Imagery that is most useful in a mapped display is ingested into the catalog's Maps tool (described below), provided that it is georeferenced.

SITUATIONAL AWARENESS AND REAL-TIME DECISION-MAKING. As mentioned above, the field catalog contains a tool called Catalog Maps, which allows users to overlay various products onto a mapped display with instrument locations, flight plans, etc. This tool provides excellent situational awareness and is also available on NCAR aircraft. Catalog Maps provides rapid updating of instrument locations; for NCAR aircraft, this update rate is currently at 5 s. It can show mobile vehicle locations, dropsonde and upsonde locations, winds and skew T–log$p$ diagrams, aircraft tracks, satellite, radar and lightning imagery, model forecasts, and other graphics.

Other capabilities include the provision of a real-time communications tool (IRC), expendables tracking, e-mail product submission, objective scorecards, and a preliminary data sharing service among local and remote investigators. The field catalog remains online prior to, during, and long after the field campaign ends. The field catalog is developed and maintained by EOL's Data Management and Services Facility, and catalogs for all current and completed field projects are available online (http://catalog.eol.ucar.edu/). When referencing the EOL field catalog in publications or proposals, please use its digital object identifier (https://doi.org/10.5065/D6SQ8XFB).

cloud-base heights while pointing up and cloud-top height estimates when pointing down, together with aerosol properties, derived from profiles of backscatter cross section, extinction cross section, and depolarization ratio at 532 nm at a temporal resolution of ~0.5 s. The range resolution of the retrieved backscatter cross-sectional profiles is ~30 m, while that of the extinction profile is ~300 m (Morley et al. 2012). The circular depolarization ratio observed by the HSRL can aid distinction between different aerosol types based on their aspect ratio (Burton et al. 2012). On the GV the laser transmitter and telescope can be manually oriented to face either upward or downward (see Fig. 2) through windows on the top and bottom of the fuselage.

The first three Doppler spectral moments from the HCR, and the backscatter and extinction cross sections from the HSRL were combined to retrieve drizzle drop size distributions while pointing up using the technique proposed by O'Connor et al. (2005). For optically thin clouds that were detected by both the HCR and the HSRL, the cloud drop size distributions were also retrieved [see Wood et al. (2018) for an example from a CSET flight].

When the aircraft was flying above the MBL in surveying mode (at a flight level of ~6 km), the HCR and HSRL were operated pointing downward to observe MBL cloud and aerosol fields from the flight level to the surface. For clouds that are 5 km below the aircraft, the HCR minimum detectable reflectivity is about –23 dBZ. On flight legs below the cloud base (near surface), the HCR and HSRL were facing upward to sample clouds and aerosols above the flight level. During the flight legs in the clouds, the HCR and HSRL were pointing downward to characterize the subcloud-layer aerosol and precipitating fields. The combined HCR and HSRL retrievals were used to estimate cloud boundaries for the flights flown (Schwartz et al. 2018, manuscript submitted to *J. Atmos. Oceanic Technol.*).

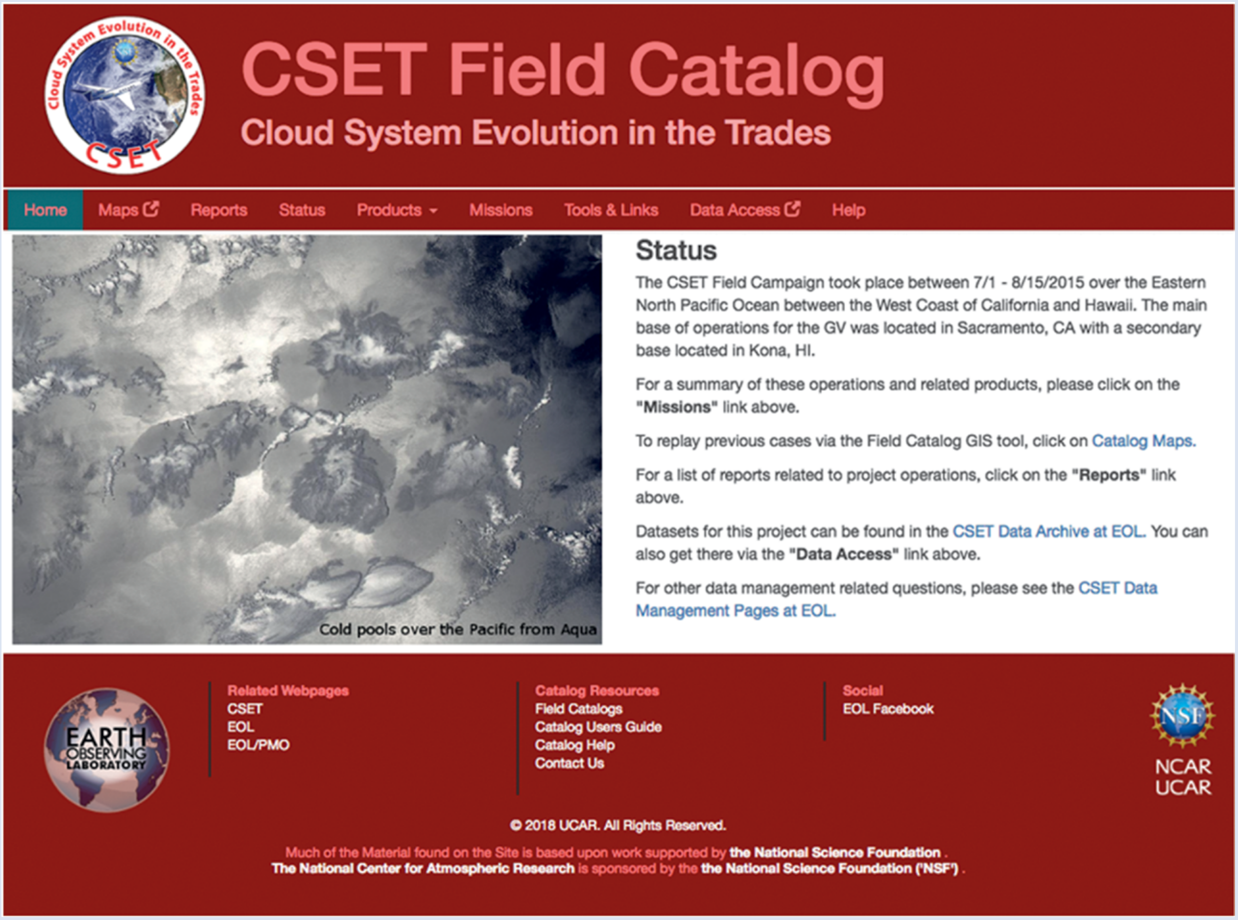

Status

The CSET Field Campaign took place between 7/1 - 8/15/2015 over the Eastern North Pacific Ocean between the West Coast of California and Hawaii. The main base of operations for the GV was located in Sacramento, CA with a secondary base located in Kona, HI.

For a summary of these operations and related products, please click on the "**Missions**" link above.

To replay previous cases via the Field Catalog GIS tool, click on Catalog Maps.

For a list of reports related to project operations, click on the "**Reports**" link above.

Datasets for this project can be found in the CSET Data Archive at EOL. You can also get there via the "**Data Access**" link above.

For other data management related questions, please see the CSET Data Management Pages at EOL.

© 2018 UCAR. All Rights Reserved.

Much of the Material found on the Site is based upon work supported by **the National Science Foundation** .
The National Center for Atmospheric Research is sponsored by the **the National Science Foundation ('NSF')** .

Fig. SB1. CSET field catalog home page.

To further complement the HCR and HSRL measurements, a multifrequency zenith-pointing radiometer was flown to provide liquid water path (LWP) and water vapor estimates. This radiometer is similar to one used during the VOCALS project (Zuidema et al. 2012b), but in addition to four channels around the 183-GHz water vapor absorption band, there is also a channel in the 90-GHz window region. Such radiometers have the potential to provide an additional fundamental cloud observation that can help connect the observations to models and quantify the cloud albedo and rain susceptibilities, or how much the cloud albedo and rain vary as a function of droplet number and LWP (Terai et al. 2012; Painemal and Zuidema 2013). Further, they can provide a geophysical constraint on lidar- and radar-specific retrievals, such as the simple reflectivity factor–liquid water content (Z–LWC) relationship for nonprecipitating clouds (dBZ < –15; Frisch et al. 1998). In this particular deployment, the radiometer did not perform as well, with inconsistent brightness temperatures between different channels. This encourages more emphasis on proper predeployment calibration procedures for future campaigns.

CSET also deployed HARP, measuring both upwelling and downwelling spectrally resolved fluxes between 350 and 2,200 nm with a spectral resolution of 3–8 nm. A recently installed updated light collector optics improves the accuracy of the measurements. Although HARP was not on a stabilized platform, the aircraft motion can be accounted for under most conditions. The above-cloud downward-looking measurements at visible and near-infrared wavelengths can be combined to produce estimates of the cloud optical depth and cloud-top effective radius following the approach of Nakajima and King (1990). This provides additional insights into the evolving cloud properties, for example, the relationship of the cloud-top effective radius to precipitation. The upwelling broadband irradiance spanning 200–3,600 nm was independently measured, and in combination with a downwelling broadband irradiance modeled on the spectral HARP irradiances, cloud albedo can be estimated.

Dropsondes were launched from the GV during CSET using an Airborne Vertical Atmospheric Profiling System (AVAPS; www.eol.ucar.edu/observing_facilities/avaps-dropsonde-system). In situ data from the sondes were transmitted back in real time from an onboard aircraft data system via radio link. Input for times and locations of the drop releases were sent from the flight scientist on the GV to the CSET home base in Sacramento, California, where an operator would send instructions to the GV to trigger the sonde launches at the designated points.

Supporting tools and observations. A key element of CSET was the field catalog (see sidebar for additional information). The field catalog was used extensively for mission planning, real-time access to aircraft observations, and satellite products during the missions, and for posting reports of mission planning, operations, and summaries. The catalog was used for documenting mission operations and serves as an archive reference for data collected during CSET. After the mission, the catalog is being used extensively in playback mode for aircraft observations and ancillary products collected during each mission.

Imagery from *Geostationary Operational Environmental Satellite-15* (*GOES-15*) observations (centered over 135°W longitude) was used to define the larger-scale (greater than 100 km × 100 km) cloud fields using near-real-time visible and infrared images [channels 1–4 (Ch1–Ch4); and high-resolution 1 km × 1 km visible imagery at nadir). Cloud property fields derived from the GOES observations were provided by the National Aeronautics and Space Administration (NASA) Langley Satellite Cloud and Radiation Property Retrieval System (SatCORPS; htpps:satcorps.larc.nasa.gov). Derived cloud properties were estimated using the methods outlined by Minnis et al. (2008) and Sun-Mack et al. (2014) and included broadband albedo, cloud-top height, cloud droplet concentrations, cloud droplet effective radius, liquid water path, and other cloud properties (see the Maps application in the EOL field catalog for a full list). The satellite products were available in near–real time from the field catalog and were instrumental for flight planning and for in-flight updates during the missions. All satellite product images produced during CSET are available in the playback mode with the Maps application in the EOL field catalog.

OBSERVING STRATEGY AND MISSION OPERATIONS. The general sampling strategy employed in CSET was to use the GV to sample clouds and MBL structures within trajectories extending westward along the southern periphery of the northeast Pacific. This Lagrangian strategy was used to sample aerosol, cloud, and MBL properties in areas upwind from the transition zone over the northeast Pacific on GV flights originating from Sacramento and ending in Kona, Hawaii. The GV and crew would then spend one day in Kona with a return flight to Sacramento two days after the outbound flight. The return (inbound) flight was planned so that GV could do low-level sampling in the same air masses that were sampled two days earlier during the outbound flights. The takeoff times for the two flights in the sequence were selected so that the air masses sampled near the middle of the California–Hawaii track were sampled at about the same local time on both the outbound and inbound flights.

Two modes of operations were implemented for the GV flights. The first—a surveying mode—included radar and lidar remote sensing of the clouds and MBL from an altitude of about 6-km (20,000 ft) altitude along transects. In this mode, dropsondes were deployed to obtain the thermodynamic and wind structures in and above the MBL upstream and downstream from the Sc-to-Cu transition zone. The second—an in situ mode—involved detailed profiling in the subcloud, cloud layer, and across the top of the boundary layer in three to four selected areas upstream and downstream of the transition zone. In the surveying mode, the MBL structures, cloud properties, and aerosol distributions were sampled using the HCR and HSRL operating in a downward-facing mode to sample from the flight level to the surface. This leg was typically flown at about 6 km (20,000 ft). Generally, in situ cloud and MBL observations were made in three to four targeted areas along these transects on profiling flight legs flown in and just above the BL over a distance of 1,500–1,800 km. For the return flights from Hawaii, trajectory analyses were used to identify air masses sampled two days earlier on the flight outbound from California. The flights between Sacramento and Kona were over a distance of about 4,000 km. The CSET field phase was planned for 1 July–15 August 2018—a time period when stratocumulus decks off the coast of California tend to be well defined.

Flight plans for the outbound flights originating from Sacramento were based on 500-m trajectory forecasts that were made using a Hybrid Single-Particle Lagrangian Integrated Trajectory model

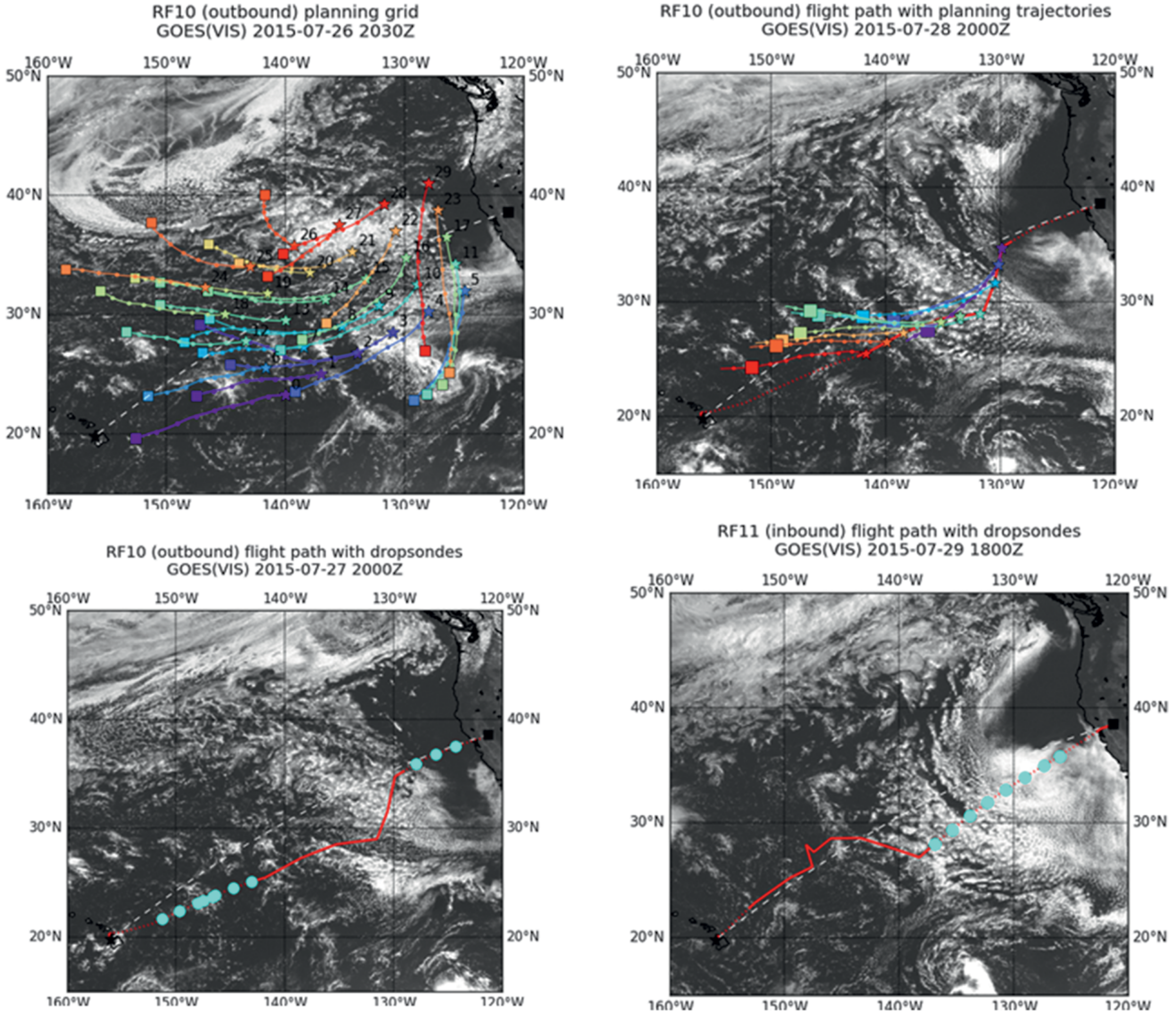

Fig. 3. Visible satellite images with trajectories used for mission planning and flight operations. White dashed line indicates a great circle from Sacramento to Kona. (top left) Trajectory swarm used on 27 Jul 2015 for RF10 flight planning, with GOES visible imagery from the morning of 27 Jul. (bottom left) RF10 flight path with dropsonde locations marked by closed circles, with GOES visible imagery from morning of 27 Jul (day of flight). (top right) RF10 flight path and RF11 planning trajectories (return flight planned through squares at trajectory ends), with GOES visible imagery from morning of 28 Jul (day between flights). (bottom right) Return flight path flown for RF11 with dropsonde locations, with GOES visible imagery for 29 Jul (day of return flight).

(HYSPLIT) with National Centers for Environmental Prediction (NCEP) Global Forecast System (GFS) forecasts and Global Data Assimilation System (GDAS) analyses. The trajectory forecasts used for the outbound planning were composed of a swarm of 28 forward trajectories released at a height of 500 m made using the 1200 UTC 0.25° forecast from the prior day's flight. The initial points for the 28 trajectories were subjectively chosen using the current GOES visible imagery to identify areas of cloud transition and were prepared for the mission planning meetings that were held in the afternoon before an outgoing flight from Sacramento the next day. An example of a trajectory swarm forecast is shown in Fig. 3 with trajectories overlain on the GOES visible imagery with the trajectory starting points for a flight planned for 27 July [research flight (RF) 10] and a return flight on 29 July (RF11). These trajectories show the starting points (stars) and the 48-h end points (squares) for the 28 trajectories.

During the mission planning meetings, the science team qualitatively examined the trajectory swarms and estimated which of the end points of these trajectories would be in the range of the GV on the return flight two days later. Initial points in areas where the greatest cloud cover was expected were identified as

Table 2. Dates for research flight couplets with latitude and longitude positions of trajectory start areas (blue circles) and end areas (red circles) two days later (see Fig. 6). Two sampling areas were identified on RF02–RF07. Three were identified on RF08–RF15.

Flight	Direction of flight	Date	Locations of air masses	Cloud fraction (%)
RF02	Westbound	7 Jul 2015	36.6°N, −136.7°E	60
			34.0°N, −141.6°E	84
RF03	Eastbound	9 Jul 2015	28.6°N, −133.9°E	67
			27.5°N, −142.6°E	25
RF04	Westbound	12 Jul 2015	31.8°N, −130.6°E	97
			28.4°N, −137.1°E	71
RF05	Eastbound	14 Jul 2015	27.9°N, −136.4°E	54
			25.0°N, −146.4°E	43
RF06	Westbound	17 Jul 2015	39.0°N, −131.5°E	100
			34.49°N, −137.0°E	91
RF07	Eastbound	19 Jul 2015	27.2°N, −140.2°E	48
			25.23°N, −149.5°E	55
RF08	Westbound	22 Jul 2015	38.1°N, −128.4°E	69
			35.9°N, −132.9°E	100
			31.7°N, −138.4°E	72
RF09	Eastbound	24 Jul 2015	28.3°N, −138.0°E	42
			28.1°N, −147.4°E	39
			25.1°N, −151.4°E	38
RF10	Westbound	27 Jul 2015	33.5°N, −129.6°E	100
			29.7°N, −133.9°E	94
			26.5°N, −140.0°E	71
RF11	Eastbound	29 Jul 2015	28.5°N, −140.4°E	92
			27.0°N, −146.8°E	44
			23.7°N, −151.5°E	35
RF12	Westbound	1 Aug 2015	42.0°N, −130.0°E	44
			40.8°N, −134.3°E	47
			38.74°N, −138.1°E	50
RF13	Eastbound	3 Aug 2015	33.5°N, −136.3°E	41
			32.2°N, −142.6°E	49
			30.02°N, −147.8°E	23
RF14	Westbound	7 Aug 2015	37.9°N, −131.9°E	56
			34.7°N, −134.7°E	90
			29.8°N, −137.8°E	70
RF15	Eastbound	9 Aug 2015	28.5°N, −141.0°E	39
			26.5°N, −148.3°E	59
			23.4°N, −151.5°E	83

candidates for sampling on the outbound flights. On this basis, the beginning points of eight trajectories in the swarm were selected as the sampling areas on the outbound flight and the 48-h trajectory end points were set as tentative sampling areas for the return flight. These flight plans were then shared with the GV pilots, who would assess the feasibility of the proposed flights and would suggest any modifications needed to make the planned flights achievable. Model forecast errors tended to have minimal effect on the trajectory forecasts, since the position and the strength of the subtropical cyclone in the study area evolve slowly with time. While errors in the analyses used to define the initial trajectories can lead to uncertainties in the trajectory paths, a qualitative assessment of the trajectories' projections compared with the 48-h movement of cloud features indicated good agreement.

After the GV landed in Kona, there was another mission planning meeting the following day. During this meeting, updated trajectory end points were used to set the flight track back to Sacramento, using 1200 UTC day-before-return-flight analysis and forecasts and the outbound flight path. The takeoff times for the two flights in the sequence were selected so that the air masses sampled near the middle of the California–Hawaii track were sampled at about the same local time on both the outbound and inbound flights. The takeoff time from California was nominally at 0800 LT, while the takeoff time from Hawaii was 0630 LT. This approach minimized diurnal effects for the middle segments of the flight. But any diurnal effects were unavoidable for the other segments of the flight.

The trajectories shown in Fig. 3 define the RF10 outbound and RF11 inbound flight plans. The beginning and end points of the eight trajectories selected for the sampling sequence are shown in Fig. 3c. These trajectories are overlaid on the satellite image from 28 July to show (after the fact) how the selected trajectories lined up with the clouds observed one day after the outgoing flight. Any minor updates to the flight plan based on subsequent forecast changes were relayed to the pilots 4 h before takeoff based on the 0600 UTC day-of-flight forecasts. For the RF10 and RF11 example sequence, the actual flight paths flown are shown in Figs. 3b and 3d, respectively, along with the satellite images of the different days of the aircraft operation. This same mission planning procedure was used for all seven flight pairs (dates tabulated in Table 2) that were made during CSET. The detailed flight paths and field reports for each of the missions can be found in the CSET field catalog.

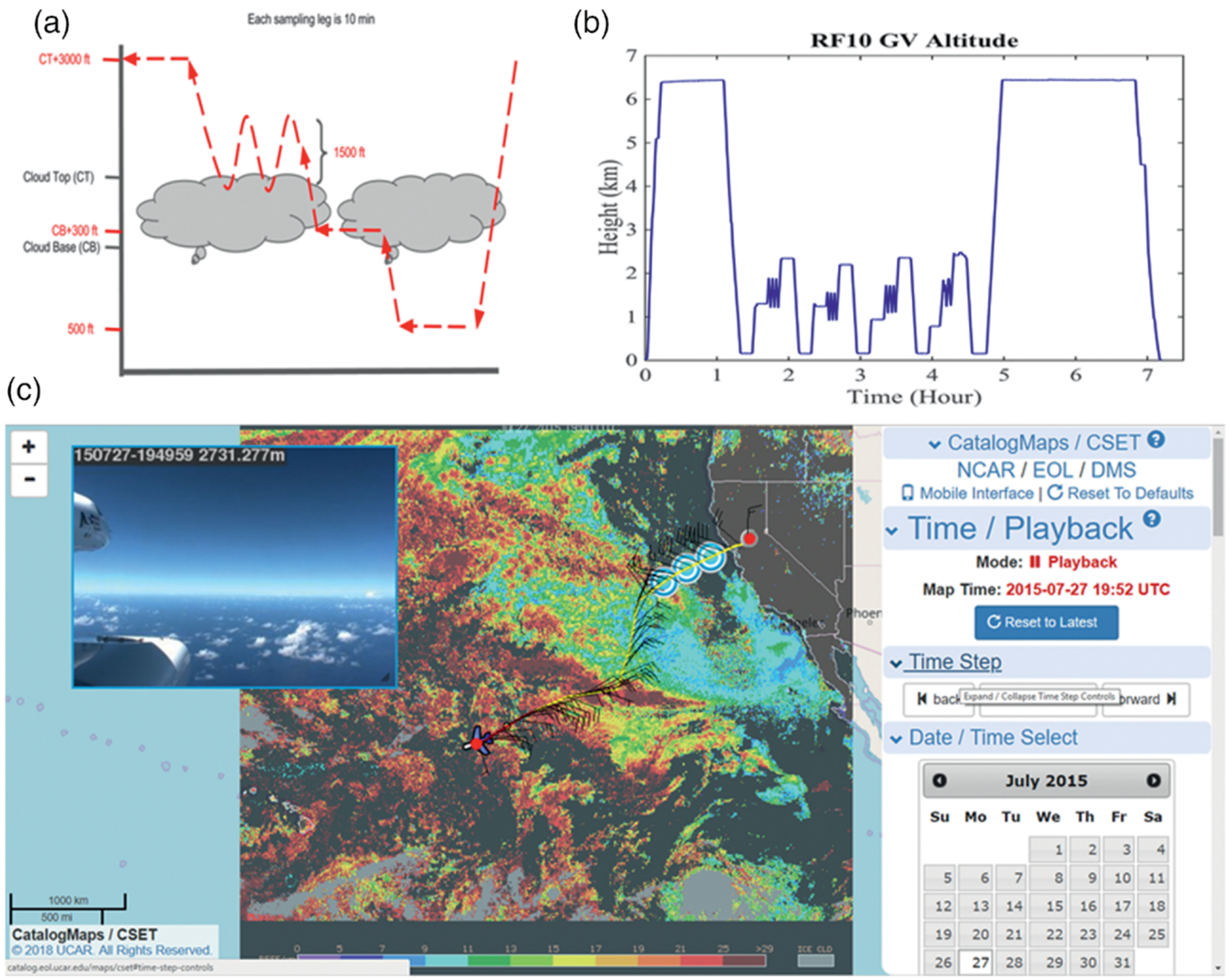

Fig. 4. (a),(b) Flight pattern plan for low-level sampling legs. Level legs are typically 8–10 min in duration. (c) Screen shot of the display from EOL field catalog II during RF10, at 1042 UTC 27 Jul 2015. Yellow line shows flight path with wind barbs overlain on the high-resolution GOES visible image and (inset) the real-time photo from a camera mounted on the starboard/right wing of GV.

The basic flight pattern planned for the low-level sampling segments for all of the flights is shown in Fig. 4. The first segment started with a descent from the surveying leg at 20,000 ft (about 6 km) to about 500 ft (150 m). This descent provided a pseudosounding, since the aircraft moves horizontally during the 20,000-ft descent. Then a level leg was flown at 500 ft for about 10 min. After this low-level leg, the aircraft ascended to about 300 ft (100 m) above the cloud base for another 10-min leg. During this leg and at 300 ft, the HCR and the HSRL beams were pointed upward. After the in-cloud leg, the aircraft would do an alternating ascent–descent sequence (sawtooth sequence) with a vertical range of about 1,500 ft (500 m) to sample the cloud top and the stable layer that often caps the cloud. This sawtooth sequence was followed by a level flight leg flown 2,000–3,000 ft above the cloud top for about 10 min. During the sawtooth and the above-cloud leg, the HCR and HSRL beams were pointed downward. Following the above-cloud leg, the aircraft descended to 500 ft and repeated the profiling sequence. The GV time–altitude plot for RF10 in Fig. 4 shows the high-level surveying legs at the beginning and end of the flight and a sequence of four low-level profiling sequences in the midsection of the flight. The flight plan was flexible so that modifications could be made during the aircraft sampling as dictated by local cloud and meteorology conditions.

Mission planning and mission control were done from the Department of Atmospheric Sciences at the University of Washington, and the aircraft home base was in Sacramento, where the EOL flight crew and technicians were located with the airborne mission scientists. Daily mission briefing and planning meetings were held at the University of Washington and networked to facilities at the Sacramento location and to Kona when the aircraft was there.

Flight operations of each mission started with preparation of the aircraft and scientific equipment about 4 h before takeoff. The flight crew consisted of two pilots, three technicians on board the aircraft, the mission scientist, and at least one additional scientist/observer. Once airborne, the mission scientist would direct the aircraft sampling sequence during the low-level profile flights and would set the dropsonde points along the surveying parts of the flight. Scientists on the ground could monitor the aircraft operations and view data in near–real time along with GOES satellite products using the satellite-linked field catalog. A real-time communications tool [Internet Relay Chat (IRC)] allowed communication among the airborne scientists, engineers and technicians, and CSET participants at the surface sites. These real-time exchanges facilitated any modification of the aircraft sampling areas and procedures, and made full use of the many eyes that were monitoring the flights and the associated cloud conditions seen from satellite.

An example of the display from the field catalog work space (in replay mode) for the midpoint of the RF10 flight on 27 July is shown in Fig. 4b. In this depiction, the GV flight path with observed winds is plotted on the image of derived effective radius from the GOES analysis. Any of the satellite cloud products can be displayed in this same format and selected using a menu that appears on the field catalog display. The images from the cameras on the GV can also be viewed at the same time through the web portal to the field catalog. The dropsonde points can be plotted on the flight display. During the flight, these field catalog near-real-time displays can be made using the menu to select the fields displayed with the flight track information. In addition, the field catalog can be used to show near-real-time displays of time–height plots of the HCR and HSRL returns. Other data collected can be plotted and displayed in real time or after flights using EOL's Aeros visualization software.

OBSERVATIONAL HIGHLIGHTS. A wide range of boundary layer structures and aerosol, cloud, and precipitation conditions were observed during the CSET missions that captured the cloud system evolution in the Pacific trades. The cloud systems sampled included solid stratocumulus infused with smoke from Canadian wildfires, mesoscale (100–200 km) cloud–precipitation complexes, and patches of shallow cumuli in very clean environments. Ultraclean layers were observed frequently near the top of the boundary layer and were often associated with shallow, layered veil (optically thin) clouds. The extent of aerosol, cloud, drizzle, and boundary layer sampling that was made over open areas of the North Pacific along 2-day trajectories during CSET is unprecedented and will enable focused modeling and process studies of cloud system evolution and the role of aerosol–cloud–precipitation interactions in that evolution.

Synoptic conditions during CSET were typical of summertime conditions over the northeast Pacific, although sea surface temperatures were slightly above normal. On average the center of the subtropical anticyclone was at about 43°N, 148°E during the CSET observing period (Fig. 5), which is slightly north of the climatological position. Some variations in the strength and location of the anticyclone were observed during the six weeks of observations. The sea surface temperatures (Fig. 5) in the study area were about 0.5°C above 1981–2010 base values. The mean low-level cloudiness from the GOES estimates is shown in Fig. 6. The winds and clouds in the southern parts of the observing areas were occasionally perturbed by tropical storms and cyclones moving through or near this area. These perturbations had limited impact on the CSET observations.

During CSET a total of seven sets of two-flight sequences (14 RFs; RF02–RF15; see Table 2) were flown between Sacramento and Kona during the period from 7 July to 9 August 2015. Each flight took about 7 h with about half of this time flown at the beginning and end of each flight in survey mode at a nominal height of 6 km. The middle of the flight was devoted to the level-leg sampling at low levels and the profiling described previously. Rough estimates of the mean trajectories used for flight planning during these 14 flights are shown in Fig. 5 and are overlaid on the mean SST and wind vectors from NCEP analyses. The mean trajectories go from lower to higher SSTs with downstream and upstream differences of 4°–8°C, and the mean near-surface winds decrease in speed.

Sampled areas at the beginning and end of individual trajectories for the 14 flights are overlain over the mean cloudiness from the GOES analyses shown in Fig. 6. The locations of the trajectory mapping areas shown in Fig. 6 are listed in Table 2. On the first six flights (RF02–RF07) at the beginning of the observational period, the low-level sampling time was less than on the flights made after that. Thus, the two sampling areas are specified in Table 2 for RF02–RF07 and three sampling areas are listed for RF08–RF15 when more time was used for low-level

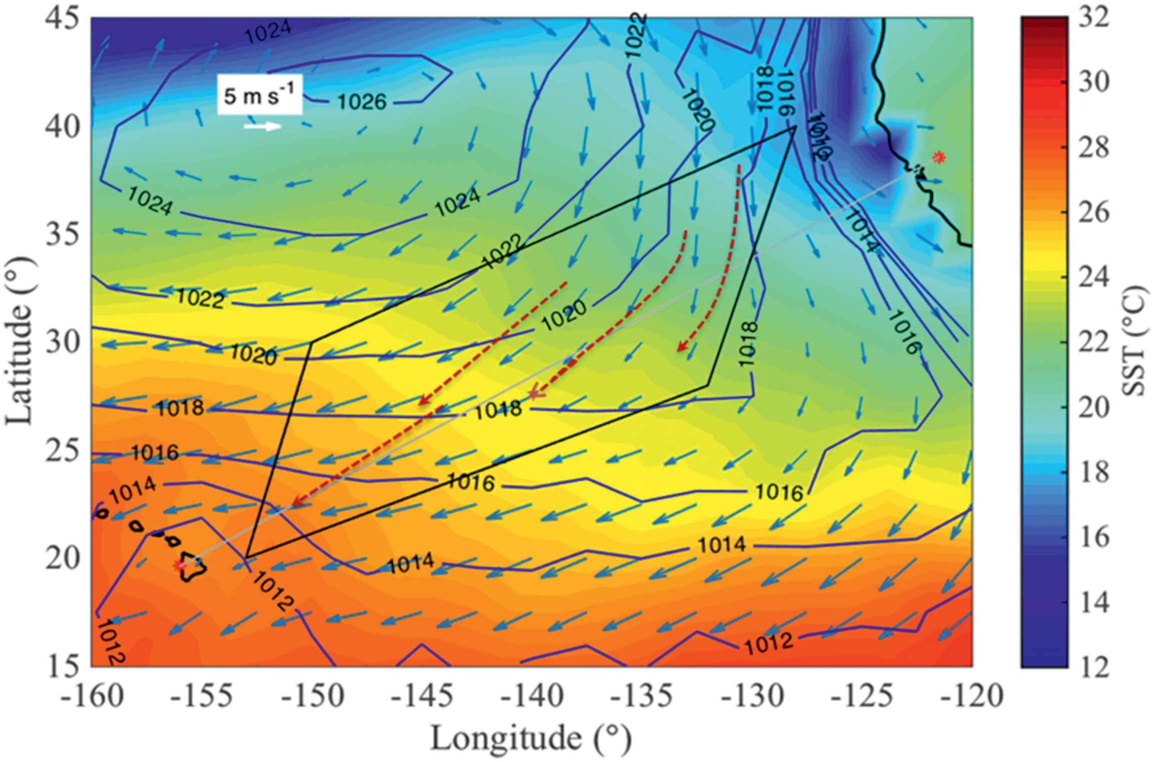

Fig. 5. Mean surface pressure (contours; hPa), SST (color shading), and surface wind vectors for CSET (6 Jul–12 Aug) from NCEP–NCAR reanalysis (Kalnay et al. 1996). Study area is indicated by the rhomboid, and trajectories represent rough means of all trajectories flown.

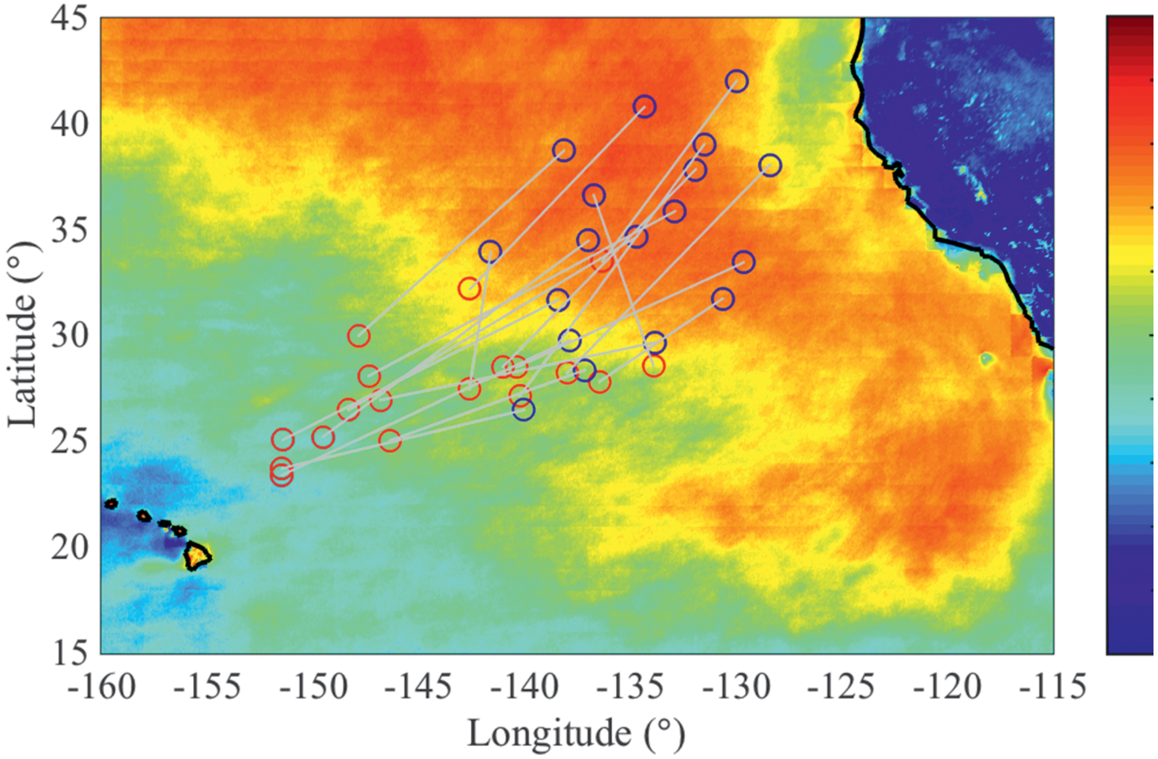

Fig. 6. Cloud fraction from GOES analyses (using Minnis et al. 2008). Blue circles are starting points of trajectory sampling areas on outbound flights from Sacramento. Red circles are areas sampled at end points of 48–52-h trajectories.

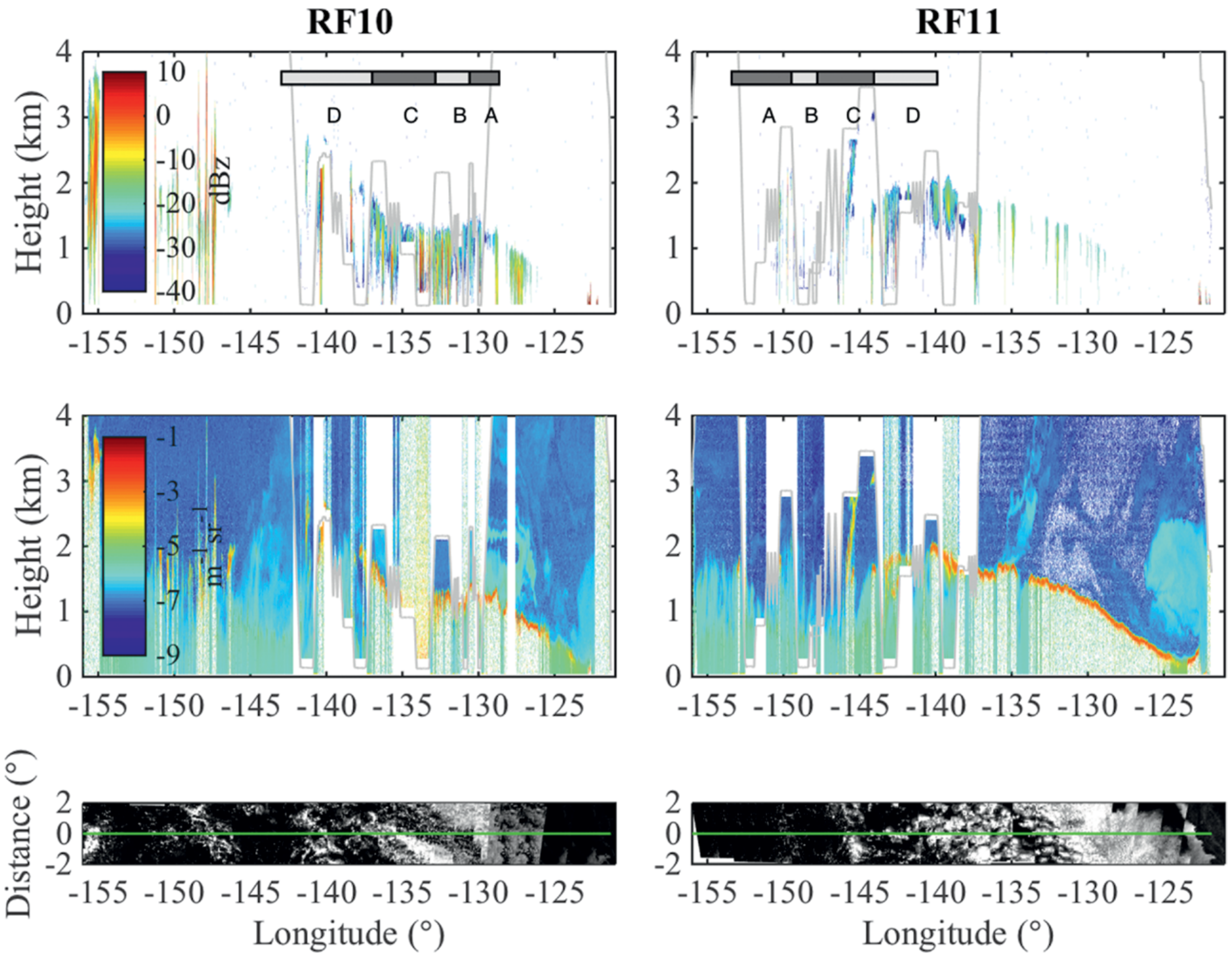

Fig. 7. (top) HCR reflectivity, (middle) HSRL backscatter, and (bottom) visible satellite image within 2° of the GV for (left) outbound RF10 on 27 Jul 2015 and (right) inbound RF11 on 29 Jul 2015. The lettered areas in the top panels correspond to one full sequence of low-level sampling. Since flights were not made in a strictly east–west orientation, the data plotted on the longitudinal axes can be relatively compressed during parts of the flight where there might be a strong north–south component to the flight path. The GV altitude is shown by gray lines in the top and middle panels.

sampling. Most of the initial sampling (blue) areas in Fig. 2 are in high-cloudiness areas relative to the areas at the end points of the trajectories 48–52 h later. Cloudiness for these sampling areas was estimated using the combined radar (HCR) and lidar (HSRL) cloud fraction (Schwartz et al. 2018, manuscript submitted to *J. Atmos. Oceanic Technol.*) and is included in Table 2. The mean cloudiness for the outbound flights (trajectory beginning points) is 77%; the mean cloudiness for the inbound flights (trajectory end points) is 49% (a mean decrease of 28% in the cloudiness from the beginning to the end of the trajectories). For the seven couplets flown (14 flights), the mean decrease was about 35% on the first five couplets and 10% on the last two couplets. Thus, overall there was good sampling of the cloudiness transition.

Lagrangian evolution sample. A sample of the Lagrangian tracking of clouds and aerosols with the HCR and HSRL during the outbound RF10 (27 July 2015) and the inbound RF11 (29 July 2011) flight sequences discussed earlier (Fig. 3) are shown in Figs. 7a and 7b, respectively. The changes in the boundary layer depth with longitude are shown clearly by the HCR and HSRL returns along the outbound flight in Fig. 7a, where the depth increases from about 0.5 to 1.2 km from 124° to 130°W. From 130° to 137°W, the boundary layer depth is nearly constant at a height of about 1.2 km and then increases to about 2.5 km at 140°W. The cloudiness is substantially reduced west of 140°W.

The boundary layer is more distinctly defined by the lidar than the radar in some cases, since the survey portions of the flight were flown at a height

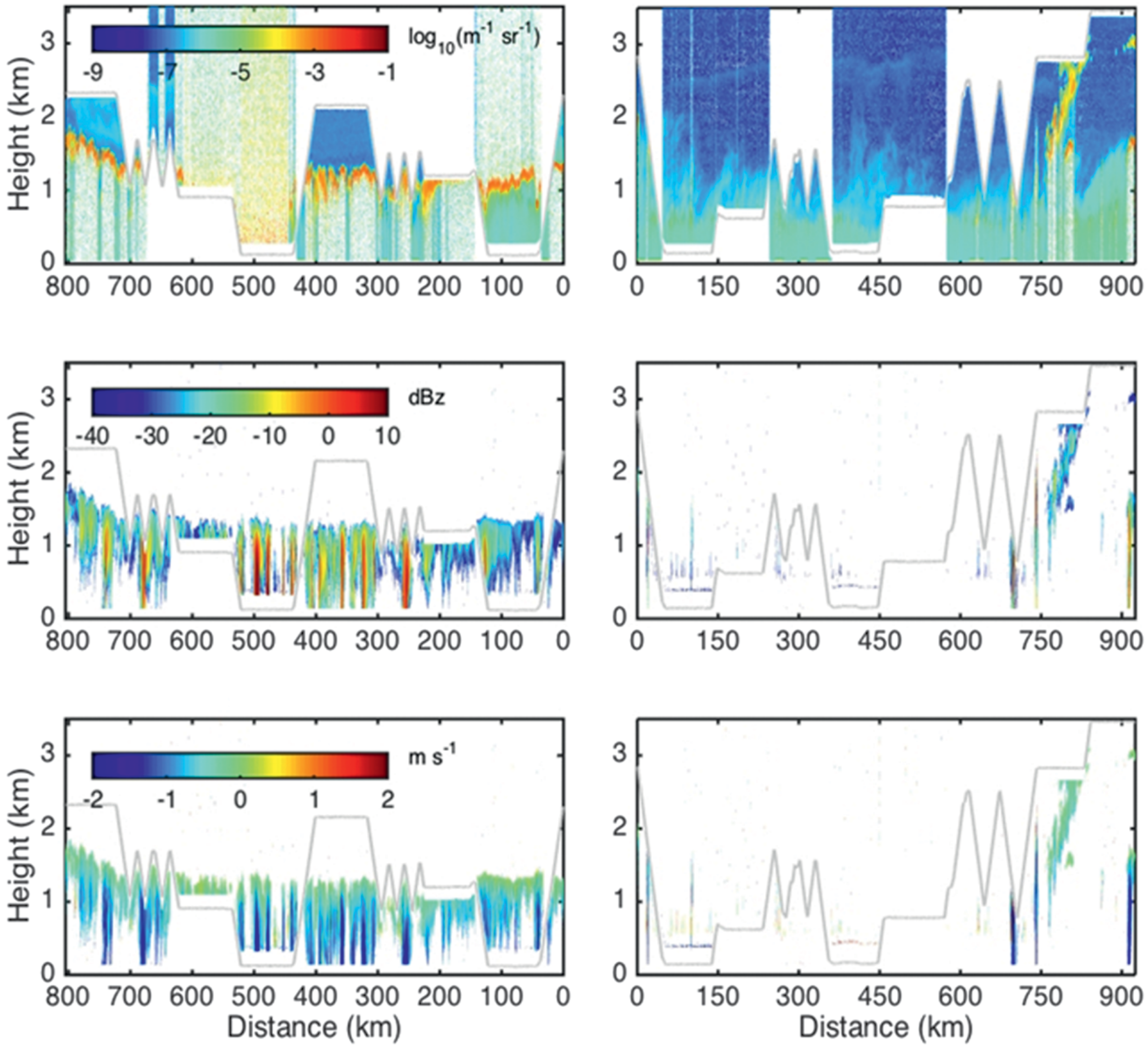

Fig. 8. (top) HSRL backscatter, (middle) HCR reflectivity, and (bottom) HCR Doppler velocity for (left) RF10 segments B–C at the beginning of trajectories and (right) RF-11 segments B–C at trajectory end points. Gray lines indicate aircraft altitude.

where the radar sensitivity is insufficient to detect low nonprecipitating thin clouds. But when flying below the cloud, the lidar is facing upward and does not detect cloud top in optically thick clouds. On the RF11 return flight, two days later the boundary layer depth is about 1.8 km from 145° to 135°W and then decreases to about 300 m at 125°W. The lidar returns in this area show mesoscale variability in the time–height aerosol structure in the planetary boundary layer (PBL). The top of the areas of enhanced backscatter are interpreted as the top of the boundary layer in this region.

The low-level sampling legs shown in Figs. 7a and 7b are segmented into the areas labeled by capital letters A–D. The segments labeled on the outbound flight sample the beginning of the trajectories selected for the mission, and the corresponding letters on the inbound flight in this case correspond to the equivalent end points of the 48–52-h trajectories. A blowup of the lidar and the radar sampling made on the B–C segments for RF10 and RF11 is shown in Fig. 8. These segments clearly show a strong change in the cloud type and amount between the beginning and end of the trajectories. After two days there is substantially less low cloud in the end of the trajectory sampling than in the beginning. There is also a notable deepening of the boundary layer from the beginning to the end of the segments. At the beginning of the trajectory sample area B–C, the radar indicates relatively solid cloud cover with drizzle and rain falling from

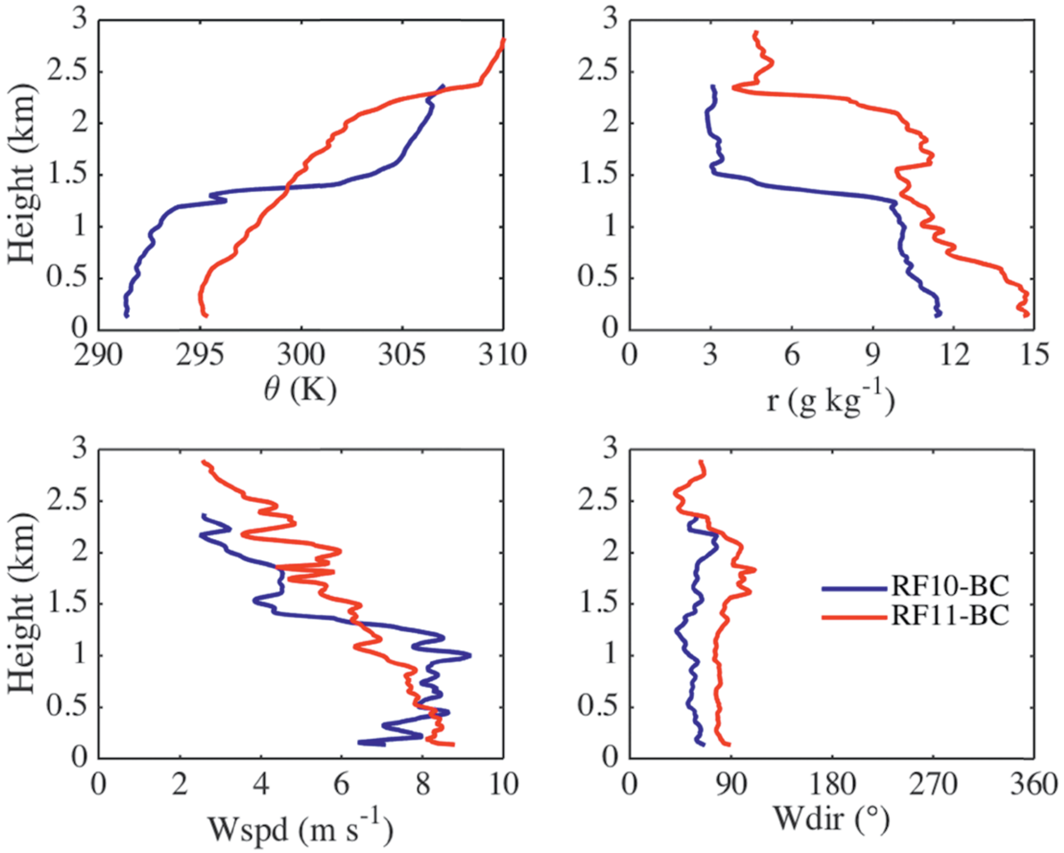

Fig. 9. (top left) Potential temperature, (top right) mixing ratio, (bottom left) wind speed, and (bottom right) wind direction as reported by in situ instruments on board GV during the ascents and descents made during RF10-B–C and RF11-B–C.

the clouds. The cloud fraction from the remote sensing measurements is about 80%. On the return flight sampling at the end of the B–C trajectories, there are relatively few clouds with a few weak echoes from small cumuli. The lidar returns in this area show mesoscale variability in the time–height aerosol structure in the PBL from 0.5- to 1.8-km altitude. This mesoscale variability may be due to processing of the aerosols by previous convective activity.

Potential temperature, mixing ratio, and wind profiles at the beginning and the end of the B–C trajectory (Fig. 9) from the aircraft measurements show the evolution of the boundary layer structure over the 2-day period. As expected, substantial warming (about a 4-K increase) and moistening (about 3 g kg^{-1}) occur over the period that are consistent with the increase in SST along the trajectory. The capping inversion defined from the soundings increases from about 1.4 km at the beginning of the trajectory to about 2.3 km at the end. The potential temperature and mixing ratio profiles show some decoupling at the beginning of the trajectory that becomes more pronounced at the end. These profiles represent a combination of vertical and horizontal variability, making interpretation of features like the moist layer observed at the top of the boundary layer ambiguous.

The seven Lagrangian pairs obtained during CSET provided an unprecedented description of the evolution of the clouds and boundary layer structures in the North Pacific trades. Although there was variability on the different days, a common feature was that on the outbound flights the boundary layer was already showing signs of decoupling in the initial sampling areas associated with stratocumulus clouds around 140°W. These decoupled stratocumulus areas were followed by areas that were dominated by mesoscale cloud systems. The classic broken fair-weather cumulus fields were not generally sampled on the outbound flights but were more prevalent at the beginning of the inbound flights originating from Hawaii. Although the boundary layer values are measured in the same air mass within the Lagrangian framework, the air above the inversion may not follow this trajectory because of the wind shear that was generally present just above the boundary layer. Regardless, the CSET trajectory analyses are a rich source of information

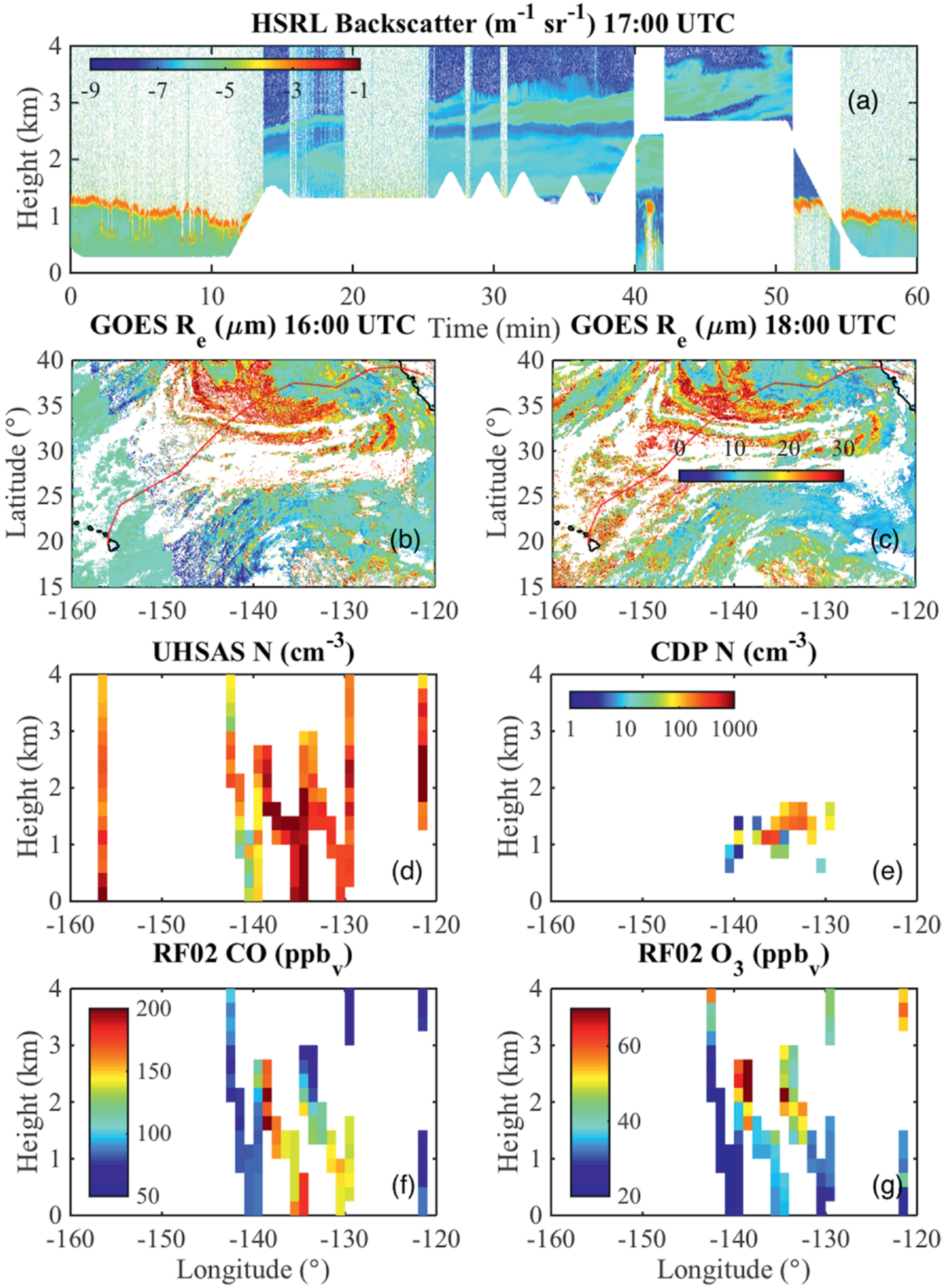

Fig. 10. (a) The HSRL backscatter on outbound flight RF02 starting at 1700 UTC 7 Jul 2015. (b),(c) The droplet effective radius from GOES analyses for the RF02 at 1600 and 1800 UTC, respectively. (d)–(g) The UHSAS-reported aerosol number concentrations, CDP-reported cloud droplet number concentrations, concentration of carbon monoxide, and concentration of ozone, respectively. The GV track for RF02 is shown in (b) and (c).

for studying the evolution of aerosols and cloud and precipitation properties in the transition process.

Process studies. The CSET observations also provide an observational basis for underlying processes involved in the evolution of the boundary layer clouds. This included illumination of the role of aerosol–cloud–precipitation interactions and the role of mesoscale cloud systems in the evolution of clouds along the trajectories sampled.

The environments sampled during some of the CSET cases showed substantial variability in the aerosols and associated cloud characteristics. An extreme example of this variability is shown for RF02 (7 July 2015), when fires in Canada produced smoke plumes that advected into the CSET sampling area and impacted clouds as shown in Fig. 10. The effective cloud droplet radius estimates from the GOES products indicate that the boundary layer clouds in the areas were affected by the smoke and showed lower effective radius values compared with those obtained in the cleaner areas to the west of the smoke-affected areas. The HSRL returns on the outbound flight RF02 also show substantial aerosol structures above the boundary layer. Enhanced CO and O_3 concentrations in the boundary layer (Fig. 10) suggest the influence of smoke in the low-level area sampled. The in situ GV aerosol concentrations (labeled UHSAS in Fig. 10) and mean cloud droplet concentrations (labeled N_D in Fig. 10) obtained on RF02 show much higher aerosol and cloud droplet number concentrations in the eastern part of the low-level sampling areas than those to the west. For a trajectory starting area sampled on the first part of the outbound RF02 flight, the boundary layer UHSAS aerosol concentrations were about 760 cm^{-3} and the concentrations above the boundary layer are about 450 cm^{-3}. In the same air mass sampled on the return flight, the boundary layer concentrations were reduced to about 410 cm^{-3} and the aforementioned inversion concentrations are about 70 cm^{-3}.

Mesoscale cloud systems in the transition area were common features observed on the CSET flights. An example of the types of systems sampled is shown in Fig. 11. These systems generally have "heavy" precipitation exceeding 10-dB*Z* reflectivity near the core of the systems with outflow clouds at the top of the system. The two mesoscale systems sampled with the HSRL and the HCR on the RF07 (19 July 2015) flight have horizontal dimensions of about 20 km and are about 60 km apart. The GOES visible image for this time period are shown in Fig. 11a. Overall, the cloud pattern shown in the satellite image can be characterized as open cells like those studied in VOCALS (Wood et al. 2011b). The core of the two systems is characterized by precipitation shafts with relatively high radar reflectivity and downward motions of about 4 m s^{-1}. Cleary defined outflow areas extend from these cores near cloud top. Although the cloud tops in the cores reach only about 2 km, the precipitation from these areas can be of sufficient intensity to give rainbows that were observed from the GV when flying at low levels (example shown in Fig. 11). The precipitation cores of the systems shown in Fig. 11 have a horizontal extent of about 5–15 km horizontally. The outflow areas in these mesoscale systems by the radar extend 20–30 km—about double that of the precipitating cloud areas.

The lidar and radar observations made in this case were taken while the GV was flying above the boundary layer. On the edges of the cloud away from the heavily precipitating cloud, the clouds are sufficiently optically thin that aerosols below the cloud can be observed with the HSRL. On the west side of the eastern cloud system, two outflow clouds at different heights are present. Both are sufficiently optically thin that the lidar penetrates both layers in some areas. These types of mesoscale cloud systems were observed on nearly all the CSET flights and clearly indicate that these systems are fundamental to the cloudiness transition observed in the CSET study area. The CSET observations provide a unique dataset for studying the heavy precipitation events observed in these clouds and the aerosol–cloud–precipitation interactions involved in these mesoscale complexes.

The mesoscale systems sampled are also rich in different types of aerosol–cloud interactions. Optically thin veil clouds that were associated with layers of very low aerosol concentrations (UHSAS concentrations < 10 cm^{-3}) near the top of the boundary layer were frequently observed during CSET. An example of these veil cloud layers and ultraclean layers is shown in Fig. 12 with the HSRL observations made on RF07. A full study of the veil clouds and the clean layers observed during CSET is given in Wood et al. (2018). They estimate that cloud cover associated with the veil clouds to be about 50% within the transition areas sampled during CSET. These clouds are both physically and optically thin. In addition to the extensive lidar and radar observations during CSET, the GV made several direct penetrations of the veil clouds during CSET that allowed for a characterization of the properties of the clouds and the aerosols in the vicinity of the clouds.

The clean layers near cloud top are clearly shown on several of the flights (Wood et al. 2018). For example, the UHSAS aerosol concentrations measured

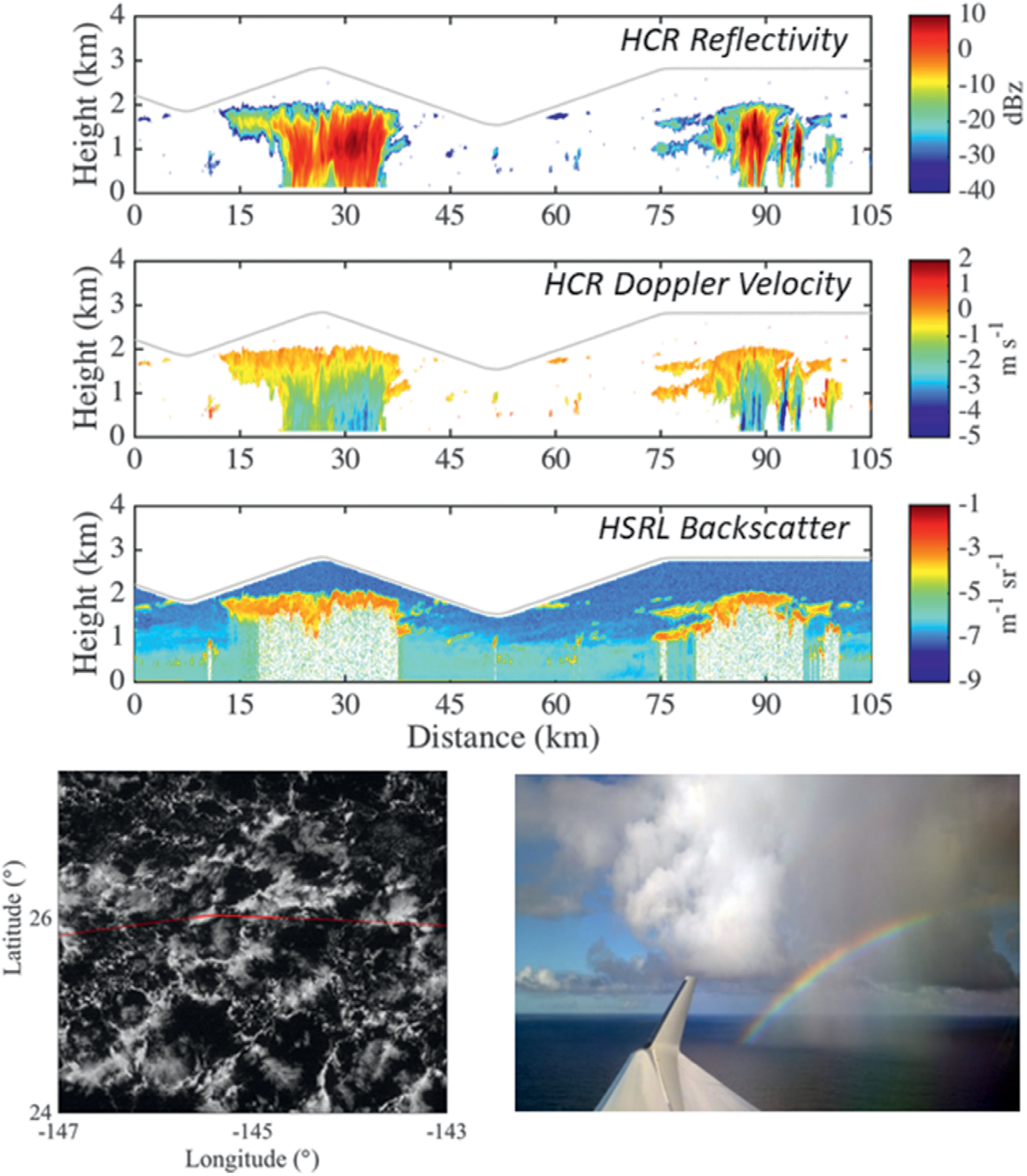

Fig. 11. (top three rows) HCR and HSRL returns from mesoscale cloud and precipitation complexes observed on RF07 during 1910–1920 UTC 19 Jul 2015. (bottom left) GOES high-definition visible image showing location of the aircraft near the time of the sampling. (bottom right) The photo of rainbow was taken on a 500-ft leg at 1802 UTC (courtesy of Jonathan Emmett).

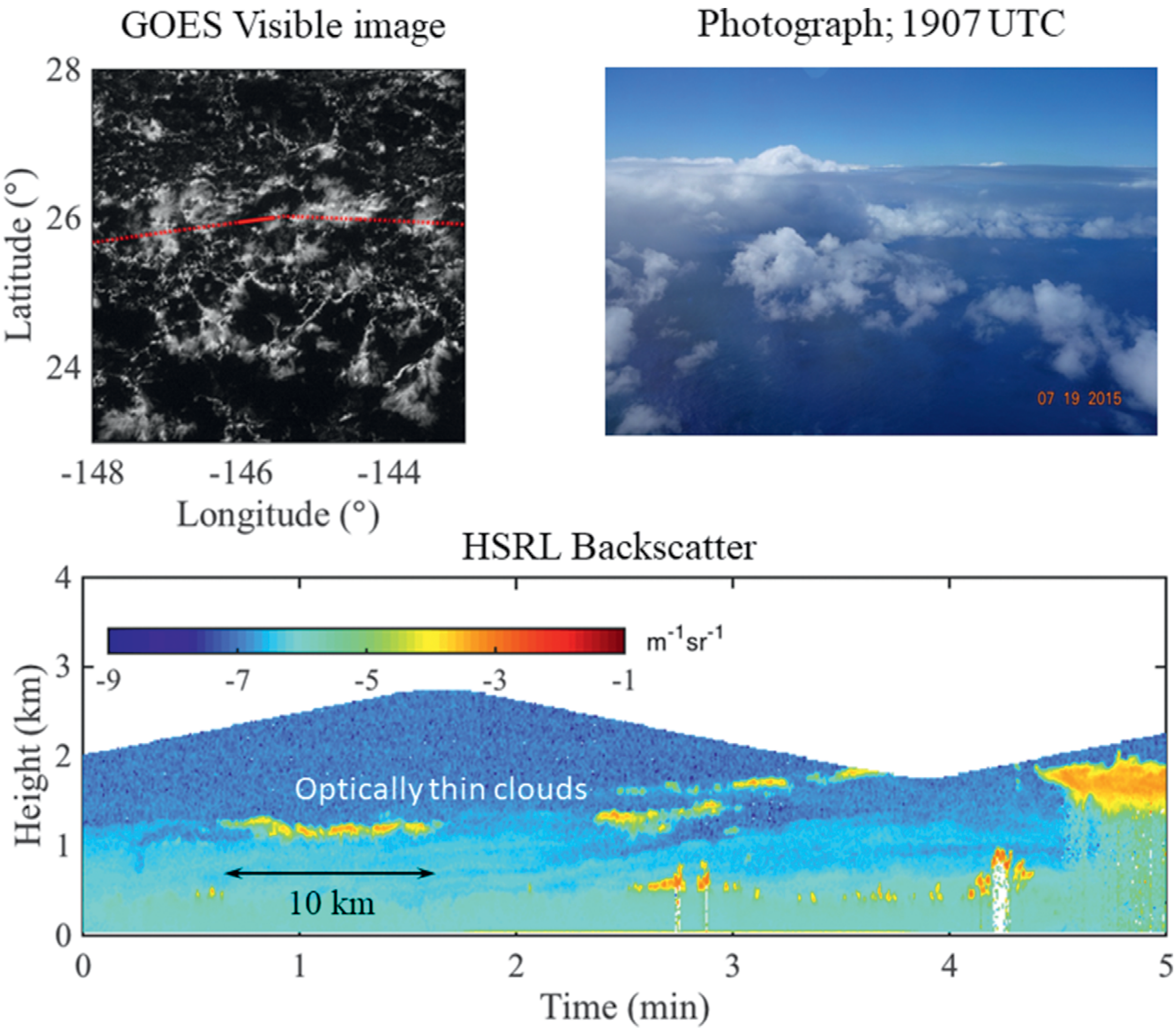

Fig. 12. (bottom) Optically thin veil clouds and ultraclean layers sampled from GV on 19 Jul 2015 by HSRL starting at 1900 UTC. (top left) A high-resolution GOES visible image and (top right) a photo taken during this time period. The GV track is overlaid on the satellite image with the solid line denoting the 5-min period corresponding to the HSRL plot. The photo was taken at 1907 UTC from GV.

on the outbound RF06 (7 July) and inbound RF07 (9 July) are shown in Fig. 13. On the outbound flight, the boundary layer aerosol concentrations vary between 100 and 300 cm^{-3}. By the time of the inbound flight, the boundary layer aerosol concentrations have been depleted to approximately 50 cm^{-3} and include a well-defined area of very low aerosol concentrations near the mean tops of clouds. The observed veil clouds and clean layers appeared to be closely coupled to mesoscale cloud systems similar to those shown in Fig. 11. A challenge will be to fully understand how the veil clouds form and their connection to the clean layers. Modeling studies are addressing these questions (Bretherton and Blossey 2017; O et al. 2018). The reduction in aerosol concentrations and deeper clouds is also reflected in larger drop sizes near cloud base, with increased subcloud evaporation over the warmer SSTs. The larger drop sizes will both deplete the cloud layer and weight the latent cooling profile closer to the surface, further aiding the Sc-to-Cu transition.

This section is intended to give a snapshot of some of the observations made during CSET. The CSET observations and the flights that were flown can be explored further by visiting the CEST field catalog.

SUMMARY. CSET made substantial advancement in our characterization of the evolution of cloud systems along the southeastern extent of the Pacific anticyclone and demonstrated the utility of a Lagrangian sampling strategy. Extensive cloud areas

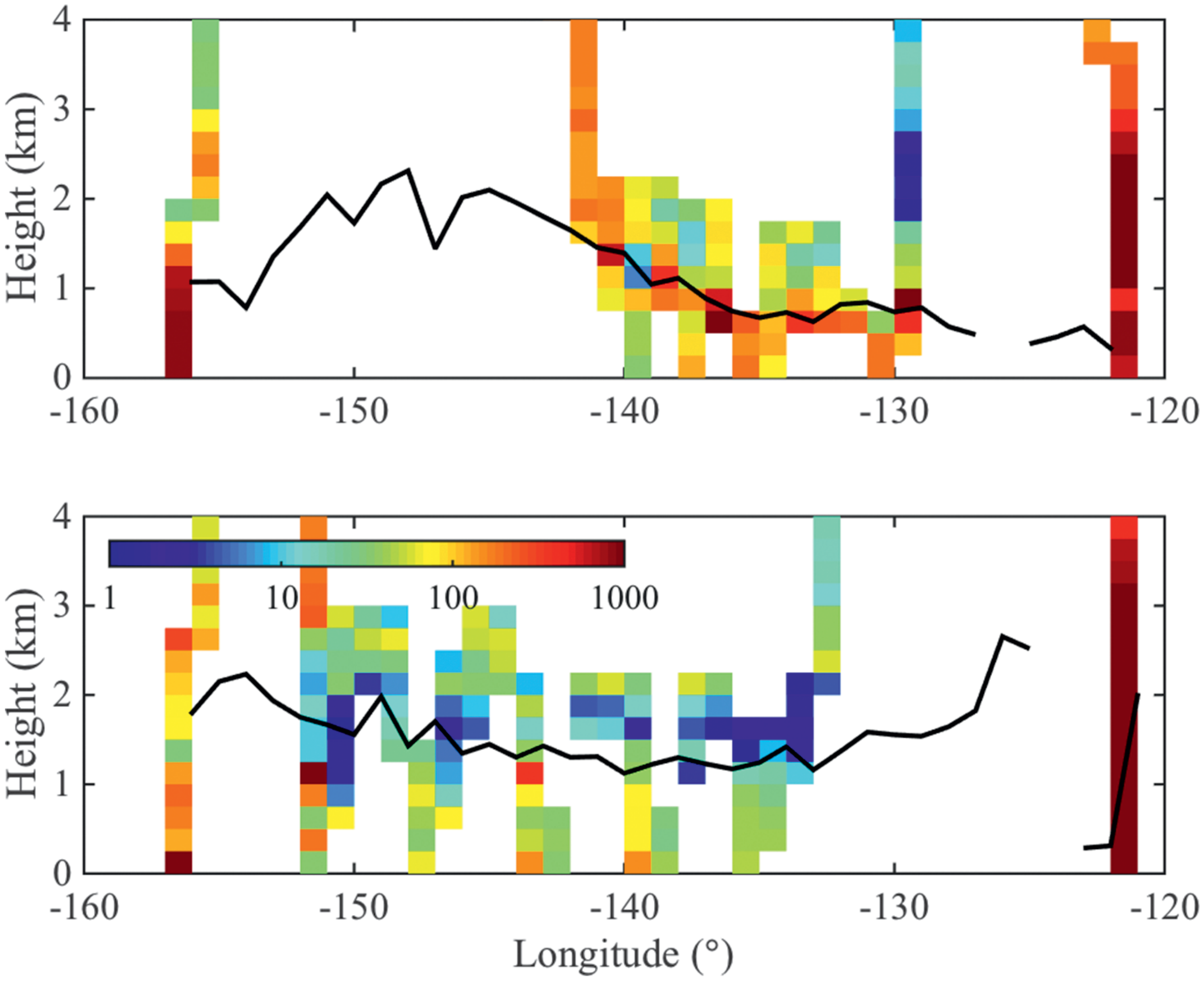

Fig. 13. UHSAS aerosol concentrations observed during (top) outbound RF06 on 7 Jul 2015 and (bottom) inbound RF07 on 9 Jul 2015 showing dominance of ultraclean layers (UHSAS concentration < 10 cm^{-3}) near cloud top on return flight RF07. The solid black lines show the cloud-top heights derived from the HCR and HSRL data. Some of the USHAS points missing below the cloud top are from samples made within the cloud, where aerosol measurements are unreliable.

were sampled and then resampled 48 h later along trajectories between California and Hawaii on seven round-trip missions involving low-level flights. These observations provide an unprecedented description of the evolution of cloud, precipitation, and aerosol fields in the cloud transition within the easterlies over the northern Pacific. The observations are being used to examine key processes governing the cloud and boundary layer properties in the transition, including the roles of large-scale forcing (e.g., sea surface temperature and winds) and cloud–aerosol–precipitation interactions. The CSET observations provide comprehensive case studies and integrated datasets to evaluate and improve process models, LES, and GCMs to describe and explain cloud system evolution in the trades.

CSET demonstrated the feasibility of a Lagrangian sampling strategy with the NSF–NCAR GV aircraft to study cloud system evolution. The range, endurance, and observational capabilities of the GV make it an ideal tool for studying shallow boundary layer clouds and mesoscale cloud systems over large domains. The HCR and HSRL remote sensing capabilities on the GV were critical to the success of CSET. They provided a detailed characterization of the structure of both precipitating and nonprecipitating clouds and the aerosol distributions above, below, and around clouds. The observing strategy employed allowed for a low-level sampling of the boundary layer over a total flight distance of about 20,000 km, and another 20,000 km of sampling made in survey mode where the radar and lidar were used to characterize clouds in the boundary layer and dropsondes were used to define boundary layer structure. There were, however, some deficiencies in the observing plan that should be addressed in future studies of this type. First, the day-2 sampling of air masses will not always be in the same local time frame as the initial measurements were made. Thus, in areas where the clouds and boundary layer may exhibit substantial diurnal variability, the Lagrangian strategy may not be ideal. Second, although the Lagrangian strategy seeks to minimize the advective effects in enthalpy and moisture budgets and for modeling studies, the air above the boundary layer will generally not follow the boundary layer because of vertical wind shear just above the boundary layer.

CSET provided enhanced learning and teaching experiences for the undergraduate and graduate students involved directly in CSET that were enabled by the use of the field catalog. Although the restricted passenger space on the GV limited the number of students who could actually fly on the missions, the field catalog allowed students to follow the progress of the CSET flights in real time and to examine the data as they were downloaded from the aircraft.

The CSET observations continue to contribute to classroom teaching and learning activities for both undergraduate and graduate students worldwide. A CSET teaching module was developed (www.eol.ucar.edu/content/cset-educational-module; http://cseteducation.weebly.com/) that allows students to experience the activities involved in carrying out a major aircraft field deployment like CSET. This module makes heavy use of EOL's CSET field catalog (http://catalog.eol.ucar.edu/cset) in playback mode (using the Maps application in the EOL field catalog) and uses GV observations for analysis exercises that can be completed by the students. The module endeavors to have students experience the types of activities involved in the field program and includes mission planning exercises. This module can also serve as a model for future EOL-related aircraft field missions.

In summary, CSET made substantial advancements in our characterization of the evolution of cloud systems along the southeastern extent of the North Pacific anticyclone. Although substantial work is in progress to analyze and use the observations made, some general features of the cloud transformation in the trades has emerged from our initial assessments. Figure 14 shows a schematic of the cloud and boundary layer evolution between California and Hawaii observed during CSET. The boundary layer undergoes a steady deepening (top increases from 500 m to 2 km) in the first 2,000 km as air moves from SSTs of 14° to 28°C. This deepening is associated with decoupling of the boundary layer and increased maximum precipitation rates. The solid clouds closest to the coast give way to mesoscale precipitating shallow cumulus complexes. These complexes produce outflow clouds at the top of the boundary that evolve into optically thin veil clouds that are associated with layers of depleted aerosols (ultraclean layers). The strength of the inversion deceases toward the west,

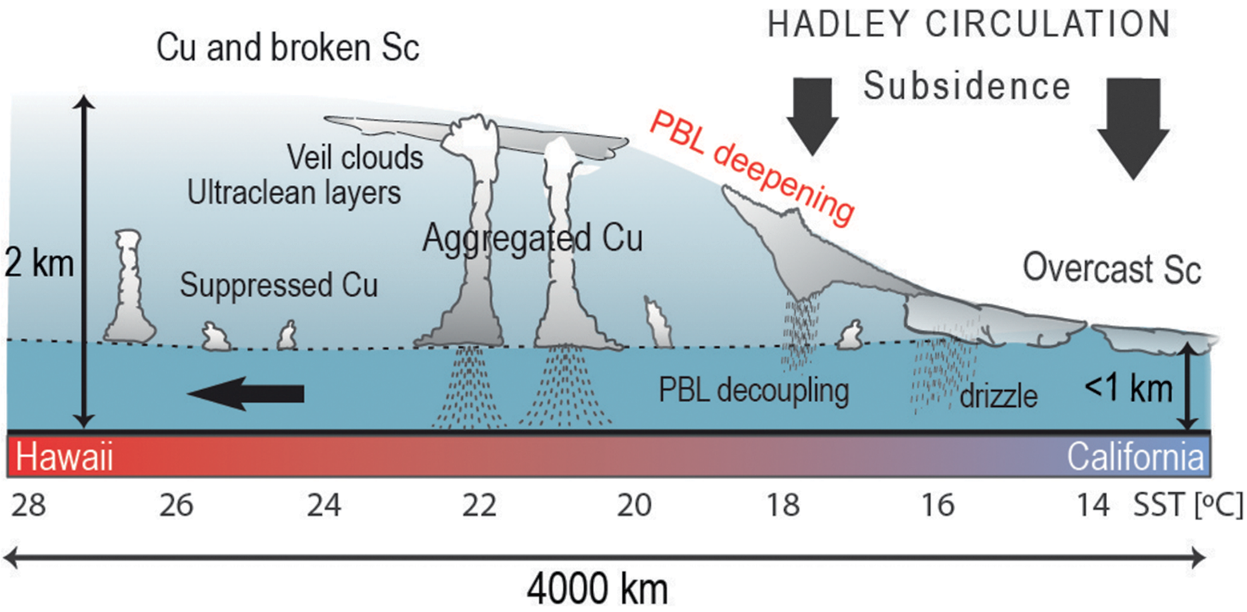

Fig. 14. Schematic showing cloud and boundary layer evolution from California to Hawaii from the CSET perspective.

although the top of the boundary layer remains at a height of about 2 km. These mesoscale complexes eventually transform to fields of cumuli that also show mesoscale organization but fewer veil clouds closer to Hawaii.

The observations will serve as a unique source of information for many future process and modeling studies that will lead ultimately to improved simulations of low-level clouds in global models. The observational techniques developed and demonstrated using the NSF–NCAR GV as an observing platform provides a firm basis for future studies of boundary layer cloud regimes using the GV.

ACKNOWLEDGMENTS. A special note of thanks and appreciation goes to NCAR Earth Observing Laboratory staff members supporting CSET for their efforts and support in the field, and a special thanks to the GV pilots, who worked diligently to accommodate our needs to make the Lagrangian flight missions possible. This research was supported by the National Science Foundation Grant AGS-1445832 to the University of Miami, Grant AGS-1445813 to the University of Washington, and Grant AGS-1445831 to the University of Chicago. V. G. was also supported by the U.S. Department of Energy's (DOE) Atmospheric System Research (ASR) program, an Office of Science, Office of Biological and Environmental Research (BER) program, under Contract DE-AC02-06CH11357 awarded to Argonne National Laboratory. We gratefully acknowledge the computing resources provided on Blues, a high-performance computing cluster operated by the Laboratory Computing Resource Center at Argonne National Laboratory. The National Center for Atmospheric Research is sponsored by the National Science Foundation. NCEP reanalysis data were provided by NOAA/OAR/ESRL/PSD, Boulder, Colorado, from its website (www.esrl.noaa.gov/psd/). Satellite observations were supported by the NASA MAP and CERES programs.

REFERENCES

Abel, J., and Coauthors, 2017: The role of precipitation in controlling the transition from stratocumulus to cumulus clouds in a Northern Hemisphere cold-air outbreak. *J. Atmos. Sci.*, **74**, 2293–2314, https://doi.org/10.1175/JAS-D-16-0362.1.

Ackerman, A. S., M. P. Kirkpatrick, D. E. Stevens, and O. B. Toon, 2004: The impact of humidity above stratiform clouds on indirect aerosol climate forcing. *Nature*, **432**, 1014–1017, https://doi.org/10.1038/nature03174.

Albrecht, B. A., R. S. Penc, and W. H. Schubert, 1985: An observational study of cloud-topped mixed layers. *J. Atmos. Sci.*, **42**, 800–822, https://doi.org/10.1175/1520-0469(1985)042<0800:AOSOCT>2.0.CO;2.

——, M. P. Jensen, and W. J. Syrett, 1995a: Marine boundary layer structure and fractional cloudiness. *J. Geophys. Res.*, **100**, 14 209–14 222, https://doi.org/10.1029/95JD00827.

——, C. S. Bretherton, D. Johnson, W. H. Schubert, and A. Shelby Frisch, 1995b: The Atlantic Stratocumulus Transition Experiment—ASTEX. *Bull. Amer. Meteor. Soc.*, **76**, 889–904, https://doi.org/10.1175/1520-0477(1995)076<0889:TASTE>2.0.CO;2.

Berner, A. H., C. S. Bretherton, and R. Wood, 2011: Large-eddy simulation of mesoscale dynamics and entrainment around a pocket of open cells observed in VOCALS RF06. *Atmos. Chem. Phys.*, **11**, 10 525–10 540, https://doi.org/10.5194/acp-11-10525-2011.

——, ——, ——, and A. Muhlbauer, 2013: Marine boundary layer cloud regimes and POC formation in an LES coupled to a bulk aerosol scheme. *Atmos. Chem. Phys.*, **13**, 12 549–12 572, https://doi.org/10.5194/acp-13-12549-2013.

Bony, S., and J. L. Dufresne, 2005: Marine boundary layer clouds at the heart of tropical cloud feedback uncertainties in climate models. *Geophys. Res. Lett.*, **32**, L20806, https://doi.org/10.1029/2005GL023851.

Bretherton, C. S., and R. Pincus, 1995: Cloudiness and marine boundary layer dynamics in the ASTEX Lagrangian experiments. Part I: Synoptic setting and vertical structure. *J. Atmos. Sci.*, **52**, 2707–2723, https://doi.org/10.1175/1520-0469(1995)052<2707:CAMBLD>2.0.CO;2.

——, and M. C. Wyant, 1997: Moisture transport, lower-tropospheric stability, and decoupling of cloud-topped boundary layers. *J. Atmos. Sci.*, **54**, 148–167, https://doi.org/10.1175/1520-0469(1997)054<0148:MTLTSA>2.0.CO;2.

——, and P. N. Blossey, 2017: Understanding mesoscale aggregation of shallow cumulus convection using large-eddy simulation. *J. Adv. Model. Earth Syst.*, **9**, 2798–2821, https://doi.org/10.1002/2017MS000981.

——, P. A. Austin, and S. T. Siems, 1995: Cloudiness and marine boundary layer dynamics in the ASTEX Lagrangian experiments. Part II: Cloudiness, drizzle, surface fluxes and entrainment. *J. Atmos. Sci.*, **52**, 2724–2735, https://doi.org/10.1175/1520-0469(1995)052<2724:CAMBLD>2.0.CO;2.

——, S. K. Krueger, M. C. Wyant, P. Bechtold, E. Van Meijgaard, B. Stevens, and J. Teixeira, 1999: A GCSS boundary-layer cloud model intercomparison study of the first ASTEX Lagrangian experiment. *Bound.-Layer Meteor.*, **93**, 341–380, https://doi.org/10.1023/A:1002005429969.

——, P. N. Blossey, and J. Uchida, 2007: Cloud droplet sedimentation, entrainment efficiency, and subtropical stratocumulus albedo. *Geophys. Res. Lett.*, **34**, L03813, https://doi.org/10.1029/2006GL027648.

——, J. Uchida, and P. N. Blossey, 2010a: Slow manifolds and multiple equilibria in stratocumulus-capped boundary layers. *J. Adv. Model. Earth Syst.*, **2**, 14, https://doi.org/10.3894/JAMES.2010.2.14.

——, R. Wood, R. C. George, D. Leon, G. Allen, and X. Zheng, 2010b: Southeast Pacific stratocumulus clouds, precipitation and boundary layer structure sampled along 20°S during VOCALS-REx. *Atmos. Chem. Phys.*, **10**, 15 921–15 962, https://doi.org/10.5194/acpd-10-15921-2010.

Brost, R. A., D. H. Lenschow, and J. C. Wyngaard, 1982a: Marine stratocumulus layers. Part I: Mean conditions. *J. Atmos. Sci.*, **39**, 800–817, https://doi.org/10.1175/1520-0469(1982)039<0800:MSLPMC>2.0.CO;2.

——, J. C. Wyngaard, and D. H. Lenschow, 1982b: Marine stratocumulus layers. Part II: Turbulence budgets. *J. Atmos. Sci.*, **39**, 818–836, https://doi.org/10.1175/1520-0469(1982)039<0818:MSLPIT>2.0.CO;2.

Burton, S. P., and Coauthors, 2012: Aerosol classification using airborne high spectral resolution lidar measurements—Methodology and examples. *Atmos. Meas. Tech.*, **5**, 73–98, https://doi.org/10.5194/amt-5-73-2012.

Caldwell, P., and C. S. Bretherton, 2009: Large eddy simulation of the diurnal cycle in southeast Pacific stratocumulus. *J. Atmos. Sci.*, **66**, 432–449, https://doi.org/10.1175/2008JAS2785.1.

de Roode, S. R., and Coauthors, 2016: Large-eddy simulations of EUCLIPSE–GASS Lagrangian stratocumulus-to-cumulus transitions: Mean state, turbulence, and decoupling. *J. Atmos. Sci.*, **73**, 2485–2508, https://doi.org/10.1175/JAS-D-15-0215.1.

Eloranta, E. W., I. A. Razenkov, J. Hedrick, and J. P. Garcia, 2008: The design and construction of an airborne high spectral resolution lidar. *Proc. 2008 IEEE Aerospace Conf.*, Big Sky, MT, IEEE, 6 pp., https://doi.org/10.1109/AERO.2008.4526390.

Fang, M., B. Albrecht, E. Jung, P. Kollias, H. Jonsson, and I. PopStefanija, 2017: Retrieval of vertical air motion in precipitating clouds using Mie scattering and comparison with in situ measurements. *J. Appl. Meteor. Climatol.*, **56**, 537–553, https://doi.org/10.1175/JAMC-D-16-0158.1.

Frisch, A. S., G. Feingold, C. W. Fairall, T. Uttal, and J. B. Snider, 1998: On cloud radar and microwave radiometer measurements of stratus cloud liquid water profiles. *J. Geophys. Res.*, **103**, 23 195–23 197, https://doi.org/10.1029/98JD01827.

Fugal, J. P., and R. A. Shaw, 2009: Cloud particle size distributions measured with an airborne digital in-line holographic instrument. *Atmos. Meas. Tech.*, **2**, 259–271, https://doi.org/10.5194/amtd-2-659-2009.

Geerts, B., and Q. Miao, 2005: The use of millimeter Doppler radar echoes to estimate vertical air velocities in the fair-weather convective boundary layer. *J. Atmos. Oceanic Technol.*, **22**, 225–246, https://doi.org/10.1175/JTECH1699.1.

Gerber, H. E., G. M. Frick, J. B. Jensen, and J. G. Hudson, 2008: Entrainment, mixing, and microphysics in trade-wind cumulus. *J. Meteor. Soc. Japan*, **86A**, 87–106, https://doi.org/10.2151/jmsj.86A.87.

Ghate, V. P., B. A. Albrecht, and P. Kollias, 2010: Vertical velocity structure of nonprecipitating continental boundary layer stratocumulus clouds. *J. Geophys. Res.*, **115**, D13204, https://doi.org/10.1029/2009JD013091.

——, M. A. Miller, and L. DiPretore, 2011: Vertical velocity structure of marine boundary layer trade wind cumulus clouds. *J. Geophys. Res.*, **115**, D23201, https://doi.org/10.1029/2010JD015344.

Giangrande, S. E., E. P. Luke, and P. Kollias, 2012: Characterization of vertical velocity and drop size distribution parameters in widespread precipitation at ARM facilities. *J. Appl. Meteor. Climatol.*, **51**, 380–391, https://doi.org/10.1175/JAMC-D-10-05000.1.

Glienke, S., A. Kostinski, J. Fugal, R. A. Shaw, S. Borrmann, and J. Stith, 2017: Cloud droplets to drizzle: Contribution of transition drops to microphysical and optical properties of marine stratocumulus clouds. *Geophys. Res. Lett.*, **44**, 8002–8010, https://doi.org/10.1002/2017GL074430.

Hartmann, D. L., and D. Short, 1980: On the use of Earth radiation budget statistics for studies of clouds and climate. *J. Atmos. Sci.*, **37**, 1233–1250, https://doi.org/10.1175/1520-0469(1980)037<1233:OTUOER>2.0.CO;2.

——, M. E. Ockert-Bell, and M. L. Michelson, 1992: The effect of cloud type on the Earth's energy balance. *J. Climate*, **5**, 1281–1304, https://doi.org/10.1175/1520-0442(1992)005<1281:TEOCTO>2.0.CO;2.

Jung, E., B. A. Albrecht, G. Feingold, H. H. Jonsson, P. Chuang, and S. L. Donaher, 2016: Aerosols, clouds, and precipitation in the North Atlantic trades observed during the Barbados Aerosol Cloud Experiment—Part 1: Distributions and variability. *Atmos. Chem. Phys.*, **16**, 8643–8666, https://doi.org/10.5194/acp-16-8643-2016.

Kalnay, E., and Coauthors, 1996: The NCEP/NCAR 40-Year Reanalysis Project. *Bull. Amer. Meteor. Soc.*, **77**, 437–471, https://doi.org/10.1175/1520-0477(1996)077<0437:TNYRP>2.0.CO;2.

Kazil, J., H. Wang, G. Feingold, A. D. Clarke, J. R. Snider, and A. R. Bandy, 2011: Modeling chemical and aerosol processes in the transition from closed to open cells during VOCALS-REx. *Atmos. Chem. Phys.*, **11**, 7491–7514, https://doi.org/10.5194/acpd-11-4687-2011.

Klein, S. A., and D. L. Hartmann, 1993: The seasonal cycle of low stratiform clouds. *J. Climate*, **6**, 1587–1606, https://doi.org/10.1175/1520-0442(1993)006<1587:TSCOLS>2.0.CO;2.

Kollias, P., B. A. Albrecht, and F. Marks Jr., 2002: Why Mie? Accurate observations of vertical air velocities and raindrops using a cloud radar. *Bull. Amer. Meteor. Soc.*, **83**, 1471–1483, https://doi.org/10.1175/BAMS-83-10-1471.

Lilly, D. K., 1968: Models of cloud-topped mixed layers under a strong inversion. *Quart. J. Roy. Meteor. Soc.*, **94**, 292–309, https://doi.org/10.1002/qj.49709440106.

Lothon, M., D. H. Lenschow, D. Leon, and G. Vali, 2005: Turbulence measurements in marine stratocumulus with airborne Doppler radar. *Quart. J. Roy. Meteor. Soc.*, **131**, 2063–2080, https://doi.org/10.1256/qj.04.131.

Luke, E. P., and P. Kollias, 2013: Separating cloud and drizzle radar moments during precipitation onset using Doppler spectra. *J. Atmos. Oceanic Technol.*, **30**, 1656–1671, https://doi.org/10.1175/JTECH-D-11-00195.1.

McGibbon, J., and C. S. Bretherton, 2017: Skill of ship-following large-eddy simulations in reproducing MAGIC observations across the northeast Pacific stratocumulus to cumulus transition region. *J. Adv. Model. Earth Syst.*, **9**, 810–831, https://doi.org/10.1002/2017MS000924.

Mechoso, C. R., and Coauthors, 2014: Ocean–cloud–atmosphere–land interactions in the southeastern Pacific: The VOCALS program. *Bull. Amer. Meteor. Soc.*, **95**, 357–37, https://doi.org/10.1175/BAMS-D-11-00246.1.

Minnis, P., and Coauthors, 2008: Near-real time cloud retrievals from operational and research meteorological satellites. *Proc. SPIE*, **7107**, 710703, https://doi.org/10.1117/12.800344.

Minor, H. A., R. M. Rauber, S. Göke, and L. Di Girolamo, 2011: Trade wind cloud evolution observed by polarization radar: Relationship to giant condensation nuclei concentrations and cloud organization. *J. Atmos. Sci.*, **68**, 1075–1096, https://doi.org/10.1175/2010JAS3675.1.

Morley, B., S. Spuler, J. Vivekanandan, M. Hayman, and E. Eloranta, 2012: Airborne and ground-based measurements with the NCAR's GVHSRL. *Proc. 16th Int. Symp. for the Advancement of Boundary-Layer Remote Sensing (ISARS 2012)*, Boulder, CO, ISARS, 68–71.

Nakajima, T., and M. D. King, 1990: Determination of the optical thickness and effective particle radius of clouds from reflected solar radiation measurements. Part I: Theory. *J. Atmos. Sci.*, **47**, 1878–1893, https://doi.org/10.1175/1520-0469(1990)047<1878:DOTOTA>2.0.CO;2.

Neggers, R., D. Neelin, and B. Stevens, 2007: Impact mechanisms of shallow cumulus convection on the tropical dynamics. *J. Climate*, **20**, 2623–2642, https://doi.org/10.1175/JCLI4079.1.

Norris, J. R., 1998: Low cloud type over the ocean from surface observations. Part I: Relationship to surface meteorology and the vertical distribution of temperature and moisture. *J. Climate*, **11**, 369–382, https://doi.org/10.1175/1520-0442(1998)011<0369:LCTOTO>2.0.CO;2.

Nuijens, L., B. Stevens, and A. P. Siebesma, 2009: The environment of precipitating shallow cumulus convection. *J. Atmos. Sci.*, **66**, 1962–1979, https://doi.org/10.1175/2008JAS2841.1.

O, K.-T., R. Wood, and C. S. Bretherton, 2018: Ultraclean layers and optically thin clouds in the stratocumulus to cumulus transition. Part II: Depletion of cloud droplets and cloud condensation nuclei through collision–coalescence. *J. Atmos. Sci.*, **75**, 1653–1673, https://doi.org/10.1175/JAS-D-17-0218.1.

O'Connor, E. J., R. J. Hogan, and A. J. Illingworth, 2005: Retrieving stratocumulus drizzle parameters using Doppler radar and lidar. *J. Appl. Meteor.*, **44**, 14–27, https://doi.org/10.1175/JAM-2181.1.

Painemal, D., and P. Zuidema, 2013: The first aerosol indirect effect quantified through airborne remote sensing during VOCALS-Rex. *Atmos. Chem. Phys.*, **13**, 917–931, https://doi.org/10.5194/acp-13-917-2013.

Rauber, R. M., and Coauthors, 2007: Rain in Shallow Cumulus over the Ocean: The RICO campaign. *Bull. Amer. Meteor. Soc.*, **88**, 1912–1928, https://doi.org/10.1175/BAMS-88-12-1912.

——, S. M. Ellis, J. Vivekanandan, J. Stith, W. Lee, G. M. McFarquhar, B. F. Jewett, and A. Janiszeski, 2017: Finescale structure of a snowstorm over the northeastern United States: A first look at high-resolution HIAPER cloud radar observations. *Bull. Amer. Meteor. Soc.*, **98**, 253–269, https://doi.org/10.1175/BAMS-D-15-00180.1.

Razenkov, I. A., E. W. Eloranta, J. P. Hedrick, R. E. Holz, R. E. Kuehn, and J. P. Garcia, 2002: A high spectral resolution lidar designed for unattended operation in the Arctic. *Proc. 21st Int. Laser Radar Conf. (ILRC21)*, Quebec, QC, Canada, ICLAS, 57–64,

Sandu, I., and B. Stevens, 2011: On the factors modulating the stratocumulus to cumulus transitions.

J. Atmos. Sci., **68**, 1865–1881, https://doi.org/10.1175/2011JAS3614.1.

——, ——, and R. Pincus, 2010: On the transitions in marine boundary layer cloudiness. *Atmos. Chem. Phys.*, **10**, 2377–2391, https://doi.org/10.5194/acp-10-2377-2010.

Soden, B. J., and G. A. Vecchi, 2011: The vertical distribution of cloud feedback in coupled ocean-atmosphere models. *Geophys. Res. Lett.*, **38**, L12704, https://doi.org/10.1029/2011GL047632.

Spuler, S. M., and J. P. Fugal, 2011: Design of an in-line, digital holographic imaging system for airborne measurement of clouds. *Appl. Opt.*, **50**, 1405–1412, https://doi.org/10.1364/AO.50.001405.

Stevens, B., 2002: Entrainment in stratocumulus-topped mixed layers. *Quart. J. Roy. Meteor. Soc.*, **128,** 2663–2690, https://doi.org/10.1256/qj.01.202.

——, J. Duan, J. C. McWilliams, M. Munnich, and J. D. Neelin, 2002: Entrainment, Rayleigh friction, and boundary layer winds over the tropical Pacific. *J. Climate*, **15**, 30–44, https://doi.org/10.1175/1520-0442(2002)015<0030:ERFABL>2.0.CO;2.

——, and Coauthors, 2003: Dynamics and Chemistry of Marine Stratocumulus—DYCOMS-II. *Bull. Amer. Meteor. Soc.*, **84**, 579–594, https://doi.org/10.1175/BAMS-84-5-579.

Sun-Mack, S., P. Minnis, Y. Chen, S. Kato, Y. Yi, S. Gibson, P. W. Heck, and D. Winker, 2014: Regional apparent boundary layer lapse rates determined from CALIPSO and MODIS data for cloud height determination. *J. Appl. Meteor. Climatol.*, **53**, 990–1011, https://doi.org/10.1175/JAMC-D-13-081.1.

Teixeira, J., and Coauthors, 2011: Tropical and subtropical cloud transitions in weather and climate prediction models: The GCSS/WGNE Pacific Cross-Section Intercomparison (GPCI). *J. Climate*, **24**, 5223–5256, https://doi.org/10.1175/2011JCLI3672.1.

Terai, C. R., R. Wood, D. C. Leon, and P. Zuidema, 2012: Does precipitation susceptibility vary with increasing cloud thickness in marine stratocumulus? *Atmos. Chem. Phys.*, **12**, 4567–4583, https://doi.org/10.5194/acp-12-4567-2012.

Tiedtke, M., 1989: A comprehensive mass flux scheme for cumulus parameterization in large-scale models. *Mon. Wea. Rev.*, **117**, 1779–1800, https://doi.org/10.1175/1520-0493(1989)117<1779:ACMFSF>2.0.CO;2.

Ulaby, F. T., R. K. Moore, and A. K. Fung, 1981: *Microwave Remote Sensing Fundamentals and Radiometry.* Vol. I, *Microwave Remote Sensing: Active and Passive*, Remote Sensing, Vol. 2, Addison-Wesley, 473 pp.

Vali, G., R. D. Kelly, J. French, H. S. D. Leon, A. McIntosh, and R. E. Pazmany, 1998: Finescale structure and microphysics of coastal stratus. *J. Atmos. Sci.*, **55**, 3540–3564, https://doi.org/10.1175/1520-0469(1998)055<3540:FSAMOC>2.0.CO;2.

van der Dussen, J. J., and Coauthors, 2013: The GASS/EUCLIPSE model intercomparison of the stratocumulus transition as observed during ASTEX: LES results. *J. Adv. Model. Earth Syst.*, **5**, 483–499, https://doi.org/10.1002/jame.20033.

Vivekanandan, J., and Coauthors, 2015: A wing pod-based millimeter wavelength airborne cloud radar. *Geosci. Instrum. Methods Data Syst.*, **5**, 117–159, https://doi.org/10.5194/gid-5-117-2015.

Wang, H., G. Feingold, R. Wood, and J. Kazil, 2010: Modelling microphysical and meteorological controls on precipitation and cloud cellular structures in Southeast Pacific stratocumulus. *Atmos. Chem. Phys.*, **10**, 6347–6362, https://doi.org/10.5194/acp-10-6347-2010.

Wang, Y., and B. Geerts, 2013: Composite vertical structure of vertical velocity in nonprecipitating cumulus clouds. *Mon. Wea. Rev.*, **141**, 1673–1692, https://doi.org/10.1175/MWR-D-12-00047.1.

Wood, R., 2005: Drizzle in stratiform boundary layer clouds. Part I: Vertical and horizontal structure. *J. Atmos. Sci.*, **62**, 3011–3033, https://doi.org/10.1175/JAS3529.1.

——, 2007: Cancellation of aerosol indirect effects in marine stratocumulus through cloud thinning. *J. Atmos. Sci.*, **64**, 2657–2669, https://doi.org/10.1175/JAS3942.1.

——, 2012: Stratocumulus clouds. *Mon. Wea. Rev.*, **140**, 2373–2423, https://doi.org/10.1175/MWR-D-11-00121.1.

——, and Coauthors, 2011a: The VAMOS Ocean-Cloud-Atmosphere-Land Study Regional Experiment (VOCALS-REx): Goals, platforms, and field operations. *Atmos. Chem. Phys.*, **11**, 627–654, https://doi.org/10.5194/acp-11-627-2011.

——, C. S. Bretherton, D. Leon, A. D. Clarke, P. Zuidema, G. Allen, and H. Coe, 2011b: An aircraft case study of the spatial transition from closed to open mesoscale cellular convection over the southeast Pacific. *Atmos. Chem. Phys.*, **11**, 2341–2370, https://doi.org/10.5194/acp-11-2341-2011.

——, and Coauthors, 2018: Ultraclean layers and optically thin clouds in the stratocumulus to cumulus transition. Part I: Observations. *J. Atmos. Sci.*, **75**, 1631–1652, https://doi.org/10.1175/JAS-D-17-0213.1.

Wyant, M. C., C. S. Bretherton, H. A. Rand, and D. E. Stevens, 1997: Numerical simulations and a conceptual model of the stratocumulus to trade cumulus transition. *J. Atmos. Sci.*, **54**, 168–192, https://doi.org/10.1175/1520-0469(1997)054<0168:NSAACM>2.0.CO;2.

——, and Coauthors, 2010: The PreVOCA experiment: Modeling the lower troposphere in the southeast Pacific. *Atmos. Chem. Phys.*, **10**, 4757–4774, https://doi.org/10.5194/acp-10-4757-2010.

Yamaguchi, T., G. Feingold, and J. Kazil, 2017: Stratocumulus to cumulus transition by drizzle. *J. Adv. Model. Earth Syst.*, **9**, 2333–2349, https://doi.org/10.1002/2017MS001104.

Zhang, M. H., and Coauthors, 2005: Comparing clouds and their seasonal variations in 10 atmospheric general circulation models with satellite measurements. *J. Geophys. Res.*, **110**, D15S02, https://doi.org/10.1029/2004JD005021.

Zhou, X., P. Kollias, and E. R. Lewis, 2015: Clouds, precipitation and marine boundary layer structure during the MAGIC field campaign. *J. Climate*, **28**, 2420–2442, https://doi.org/10.1175/JCLI-D-14-00320.1.

Zuidema, P., and Coauthors, 2012a: On trade wind cumulus cold pools. *J. Atmos. Sci.*, **69**, 258–277, https://doi.org/10.1175/JAS-D-11-0143.1.

——, D. Leon, A. Pazmany, and M. Cadeddu, 2012b: Aircraft millimeter-wave passive sensing of cloud liquid water and water vapor during VOCALS-REx. *Atmos. Chem. Phys.*, **12**, 355–369, https://doi.org/10.5194/acp-12-355-2012.

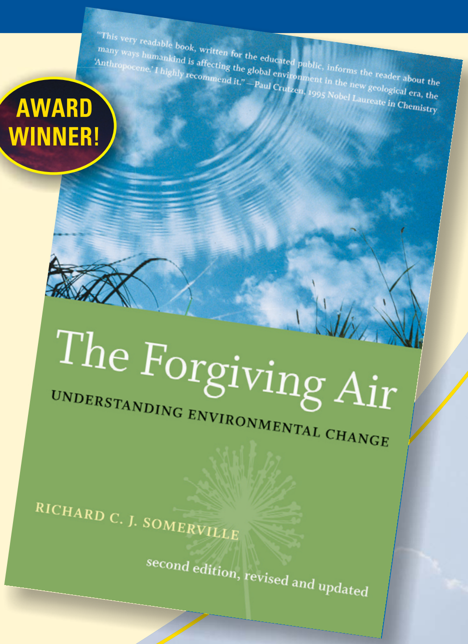

AMS Washington Forum

Connecting Science and Technology with Business and Public Policy

Save the Date

27–29 March, 2019 • Washington, DC

The 2019 AMS Washington Forum

Mark you calendars now for the 2019 AMS Washington Forum. This much-anticipated annual event provides an important platform to examine public policy issues across the weather, water and climate sciences.

This meeting is open for anyone interested in learning more about how weather, water, and climate information can help support risk management across the public and private sectors. This includes agencies and companies whose operations and planning are reliant on environmental factors.

AMS

American Meteorological Society